Supplementary Information

Molecular Design of Dual-Emission Rhodamine Analogs

Xia Wu, Ying Gao, Weijie Chi, Chao Wang, Zhaochao Xu, Xiaogang Liu*

Contents

Computation methods

For the optimization of the CT state (with charge transfer from the xanthene scaffold to phthalimidine moiety), we employed two methods: CT' was obtained via free relaxation from the Franck-Condon (FC) state; CT_1 was optimized with four constraints. These constraints afforded perpendicular alignments between the xanthene scaffold and the phthalimidine moiety, thus ensuring complete charge separation between these moieties. Upon cLR solvent effect corrections, the CT_1 state has a lower energy level and smaller oscillator strength than that of CT' state. The CT_1 yielded close agreement with experimental results. We thus chose CT_1 instead of CT' in our final analysis.
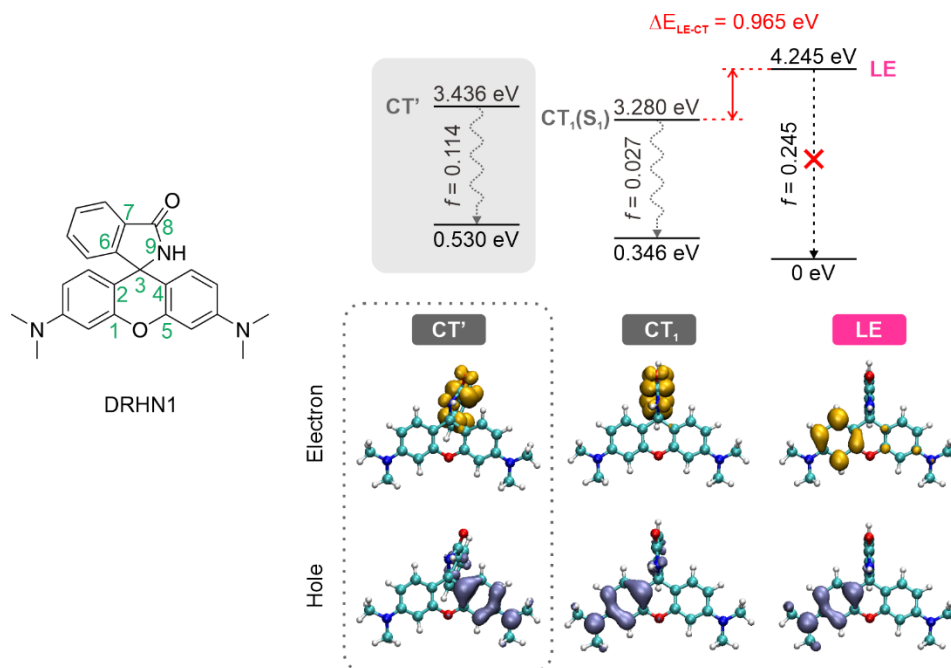
Figure S1. Molecular structure, energy levels, and the corresponding electron and hole distributions in the adiabatic excited states (AES) of DRHN1. CT' state is the charge transfer state with free relaxation from the Franck-Condon (FC) state; CT_1 state represents the charge transfer state with restricted relaxation from the FC state (the dihedral angles of 5-4-3-9, 1-2-3-6, 5-4-9-8 and 1-2-6-7 in CT_1 are fixed to the values in the FC state). LE denoted the locally excited state.

Figure S2. Molecular structure, energy levels, and the corresponding electron and hole distributions in the AES of DRHN2. The dihedral angles of 5-4-3-9, 1-2-3-6, 5-4-3-6, and 1-2-3-6 in the CT_1 state are fixed to the values in the FC state.
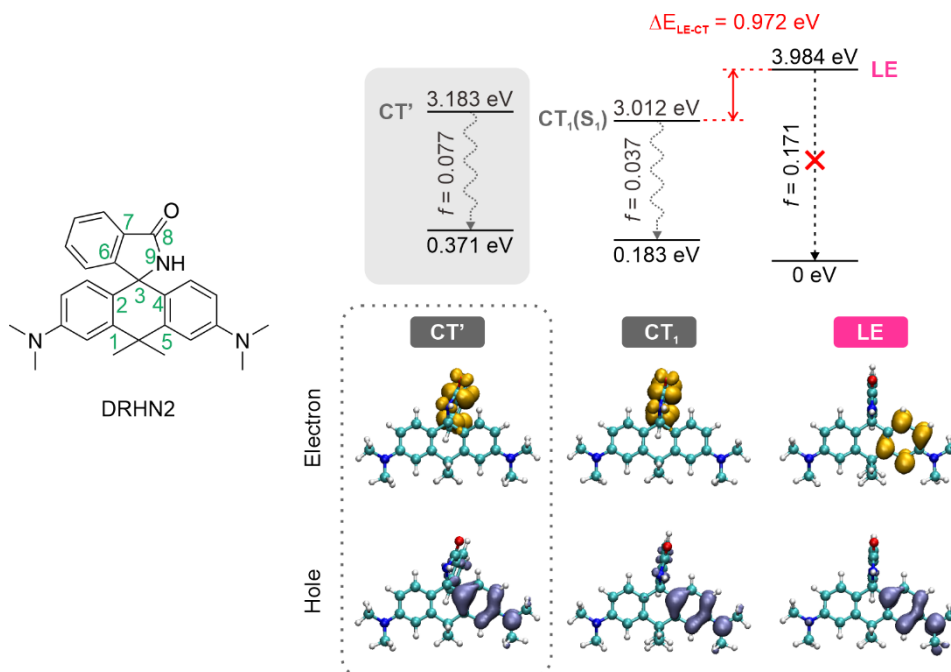
Figure S3. Molecular structure, energy levels, and the corresponding electron and hole distributions in the AES of DRHN3. The dihedral angles of 5-4-3-9, 1-2-3-6, 5-4-3-6, and 1-2-3-6 in the CT_1 state are fixed to the values in the FC state.
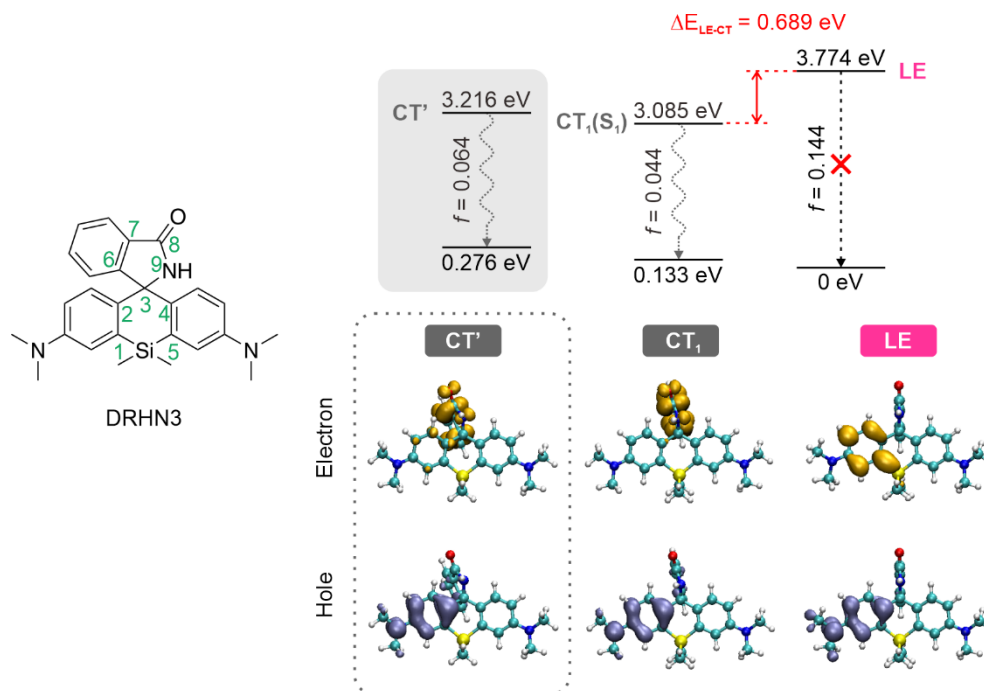

Figure S4. Molecular structure, energy levels, and the corresponding electron and hole distributions in the AES of DRHN9. The dihedral angles of 5-4-3-9, 1-2-3-6, 5-4-9-8, and 1-2-6-7 in the CT_1 state are fixed to the values in the FC state.
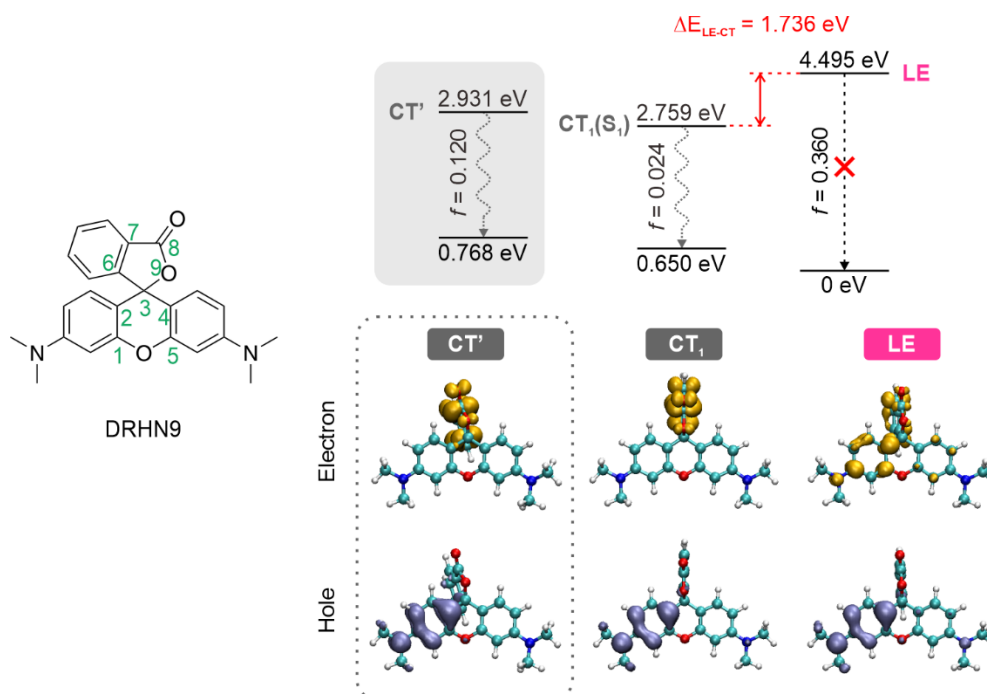
Figure S5. Molecular structure, energy levels, and the corresponding electron and hole distributions in the AES of DRHN10. The dihedral angles of 5-4-3-9, 1-2-3-6, 5-4-9-8, and 1-2-6-7 in the CT_1 state are fixed to the values in the FC state.

Figure S6. Molecular structure, energy levels, and the corresponding electron and hole distributions in the AES of DRHN11. The dihedral angles of 5-4-3-9, 1-2-3-6, 5-4-9-8, and 1-2-6-7 in the CT_1 state are fixed to the values in the FC state.
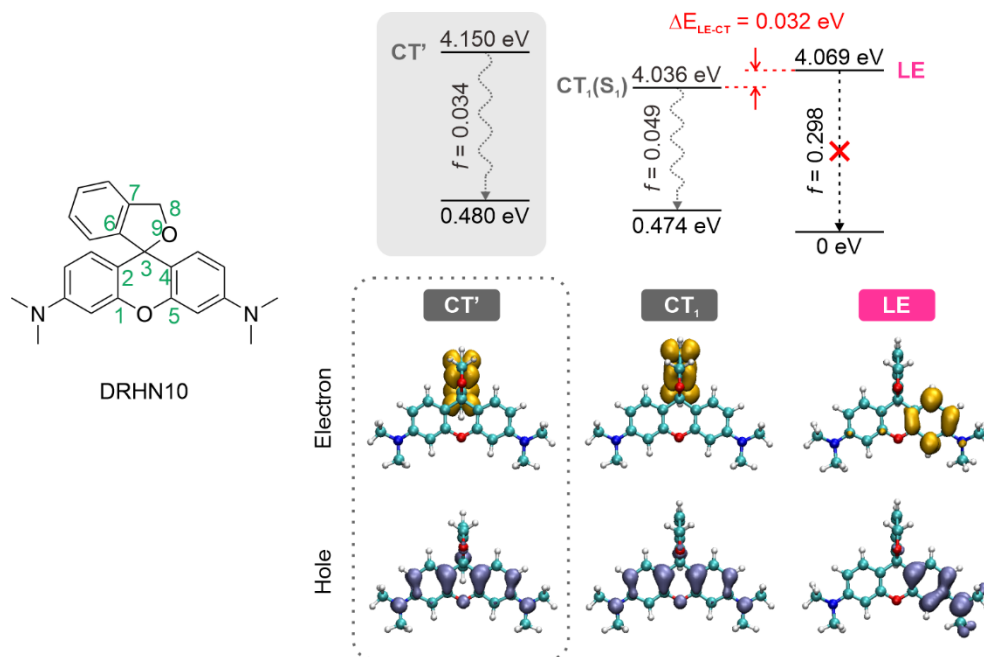
Figure S7. Molecular structure, energy levels, and the corresponding electron and hole distributions in the AES of DRHN12. The dihedral angles of 5-4-3-9, 1-2-3-6, 5-4-9-8, and 1-2-6-7 in the CT_1 state are fixed to the values in the FC state.
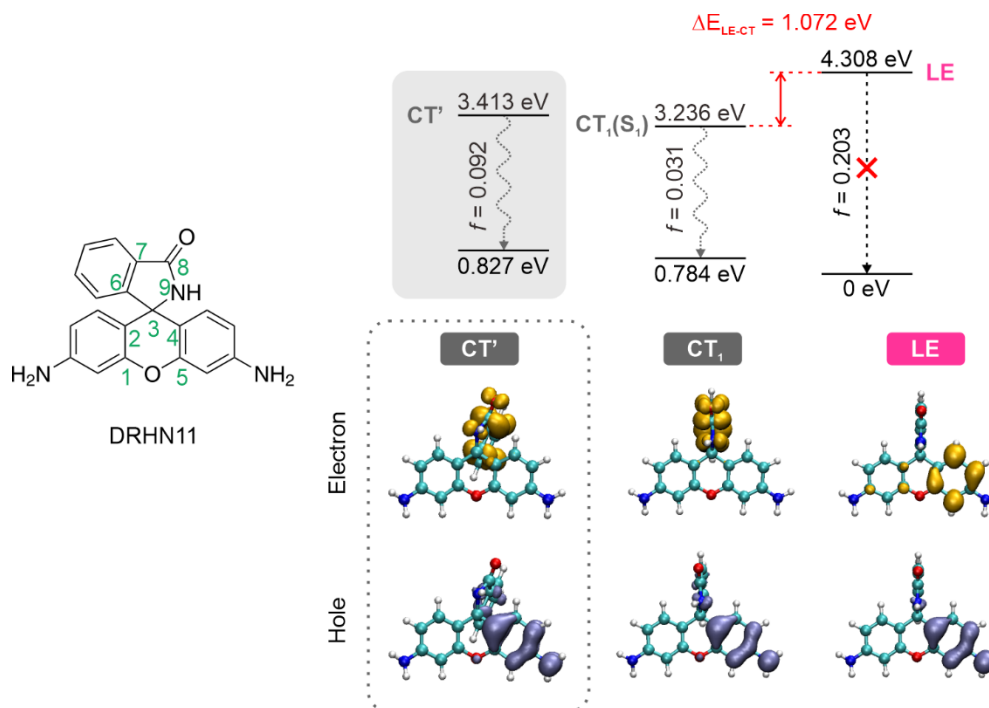

Figure S8. Molecular structure, energy levels, and the corresponding electron and hole distributions in the AES of DRHN13. The dihedral angles of 5-4-3-9, 1-2-3-6, 5-4-9-8, and 1-2-6-7 in the CT_1 state are fixed to the values in the FC state.
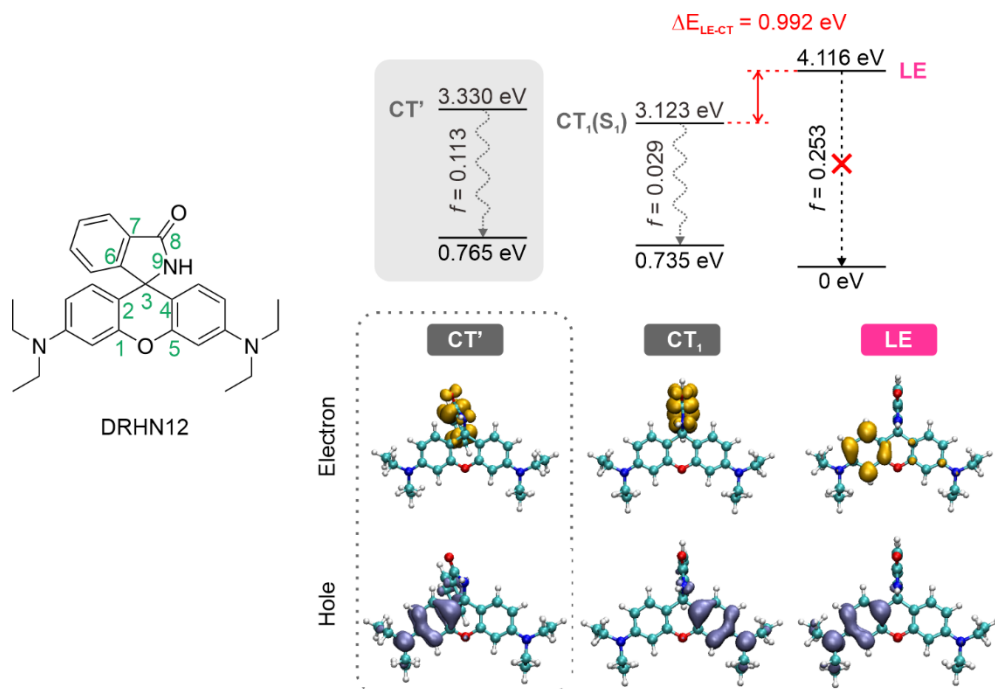
Figure S9. Molecular structure, energy levels, and the corresponding electron and hole distributions in the AES of DRHN14. The dihedral angles of 5-4-3-9, 1-2-3-6, 5-4-9-8, and 1-2-6-7 in the CT_1 state are fixed to the values in the FC state.
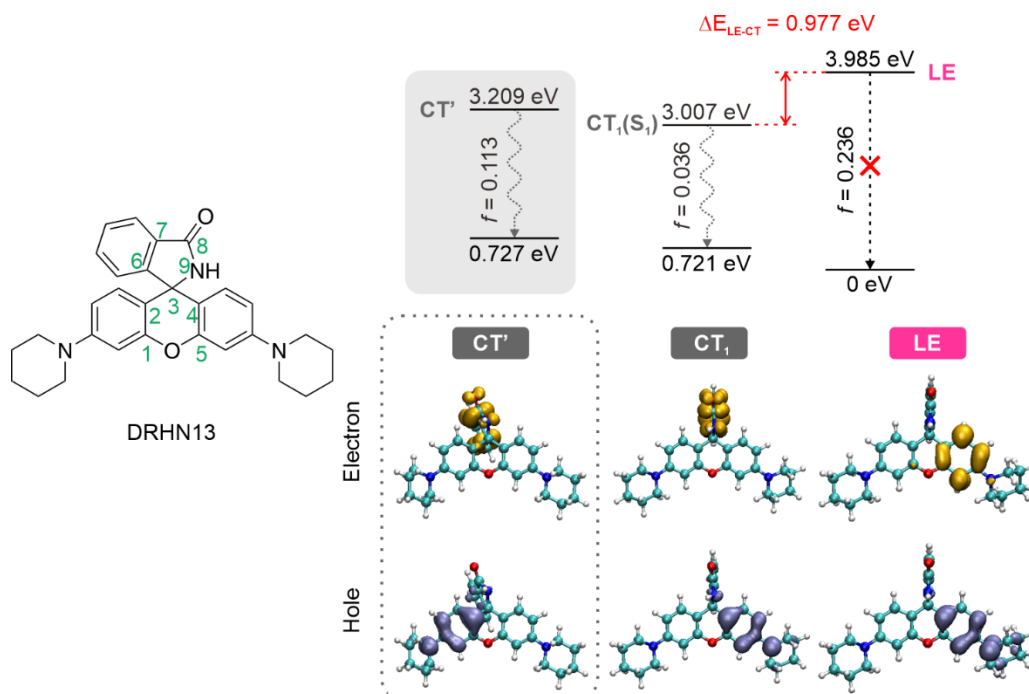

Figure S10. Molecular structure, energy levels, and the corresponding electron and hole distributions in the AES of DRHN16. The dihedral angles of 5-4-3-9, 1-2-3-6, 5-4-9-8, and 1-2-6-7 in the CT_1 state are fixed to the values in the FC state.
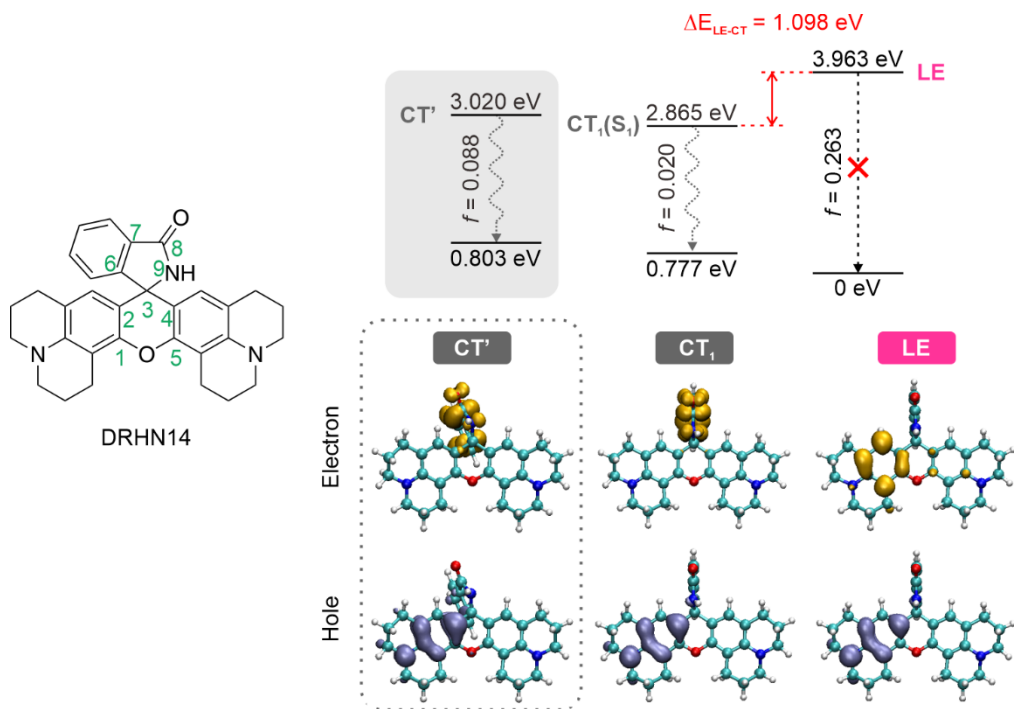
8

Figure S11. Molecular structure, energy levels, and the corresponding electron and hole distributions in the AES of DRHN17. The dihedral angles of 5-4-3-9, 1-2-3-6, 5-4-9-8, and 1-2-6-7 in the CT_1 state are fixed to the values in the FC state.
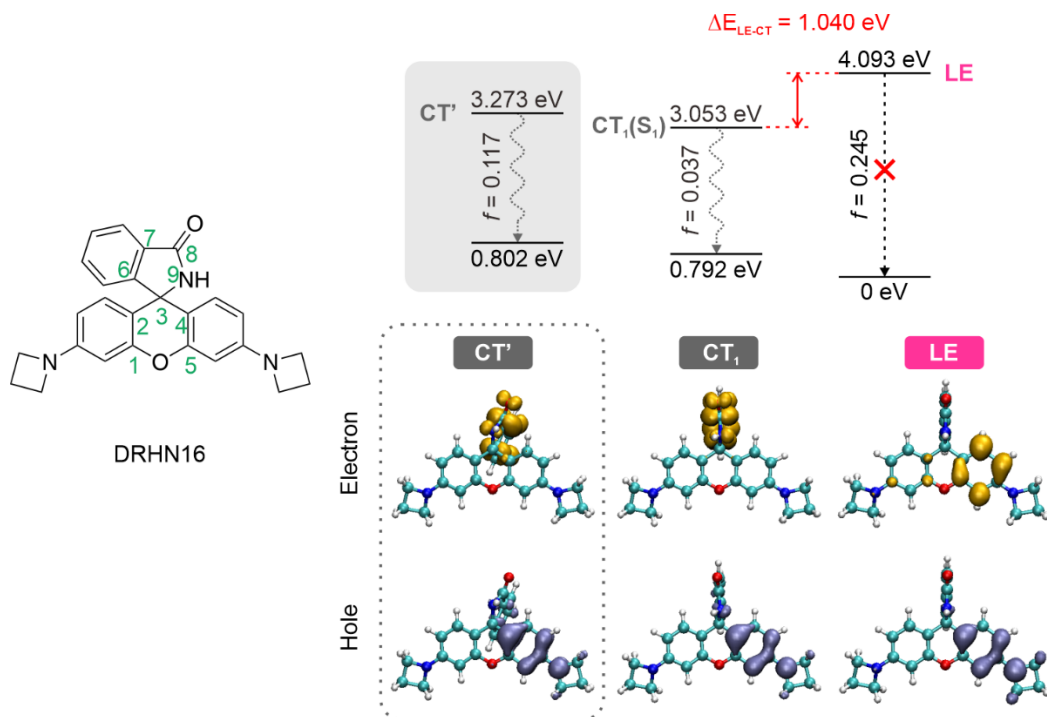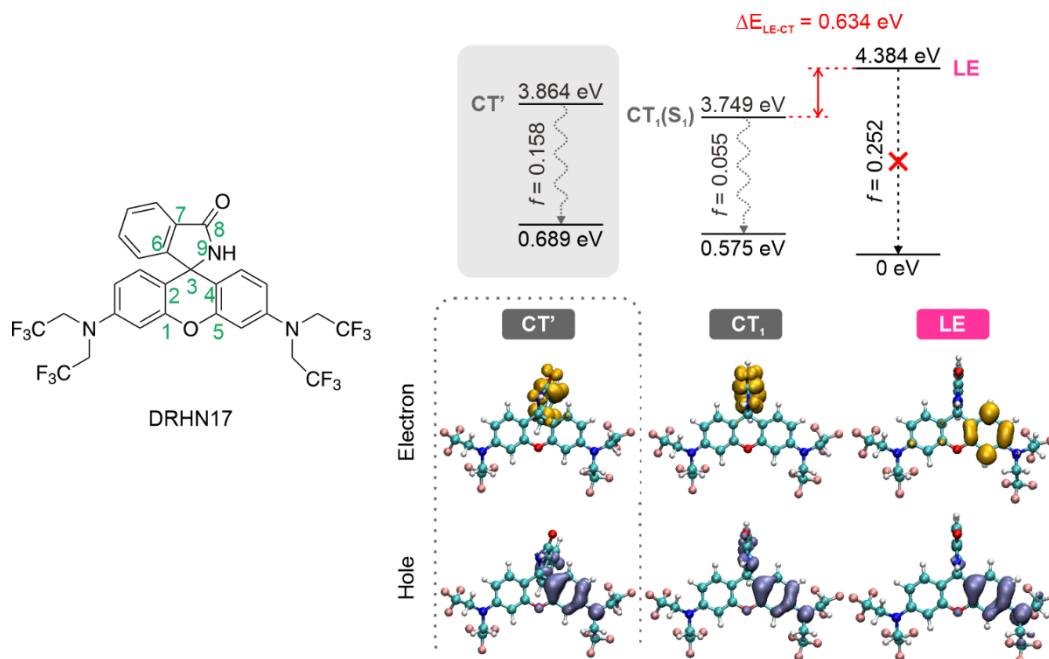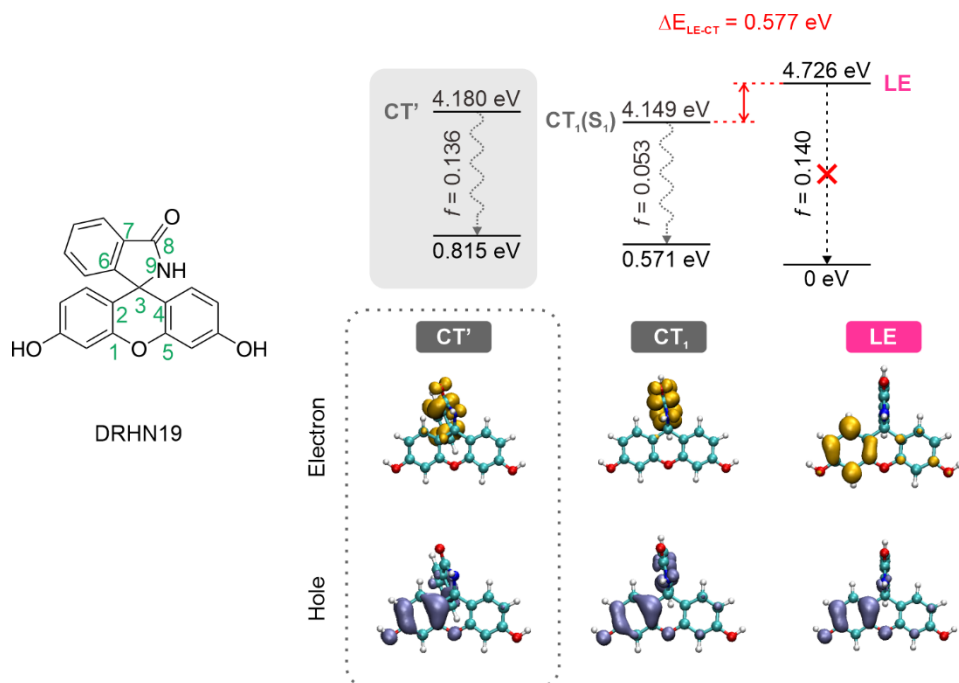

Figure S12. Molecular structure, energy levels, and the corresponding electron and hole distributions in the AES of DRHN19. The dihedral angles of 5-4-3-9, 1-2-3-6, 5-4-3-6, and 1-2-3-9 in the CT_1 state are fixed to the values in the FC state.

Figure S13. Comparison of the calculated energy levels, and the corresponding electron and hole distributions of the AES of DRHN14 using (a) M06-2X and (b) ωB97XD in combination with the def2SVP basic set in water. The constrained dihedral angles in the CT_1 state are the same as those in Fig. S9.
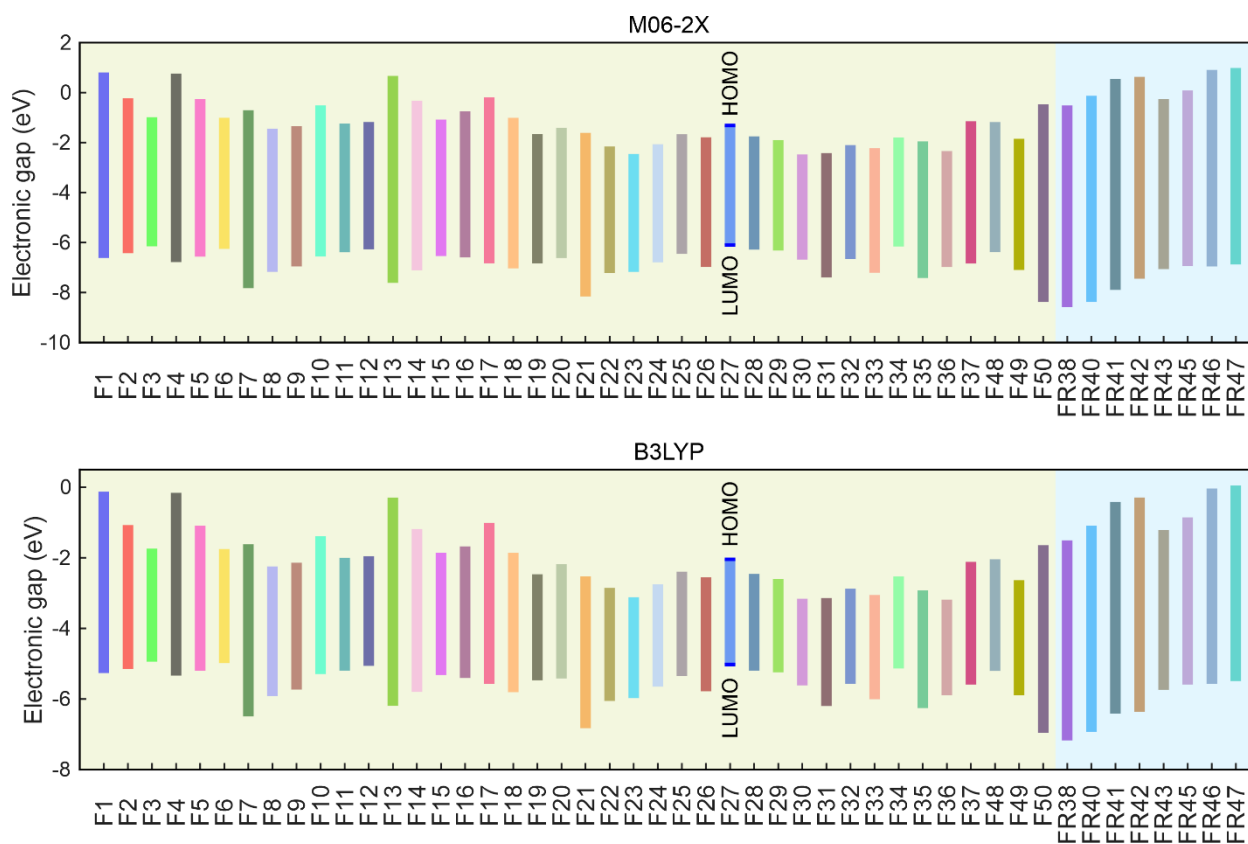
Figure S14. Calculated HOMO and LUMO energy levels in the ground state of fragments in Fig.3a using different functionals: M06-2X (top) and B3LYP (bottom) with the def2SVP basis set in water.

10

Figure S15. The molecular structure, energy levels, and the corresponding electron and hole distributions of the open form of BRHN5 in the AES.

Figure S16. (a) Three fragments, their HOMO and LUMO energy levels in the ground state, and (b) the corresponding distributions and energy levels of the molecular orbitals in the ground state of BRHN2.

Figure S17. Molecular structure, energy levels, and the corresponding electron and hole distributions in the AES of BRHN2. The dihedral angles of 5-4-3-9, 1-2-3-6, 5-4-9-8, and 1-2-6-7 in the CT_1 state are fixed to the values in the FC state. CT_2 denoted the CT state from the F1 fragment to the F3 fragment.
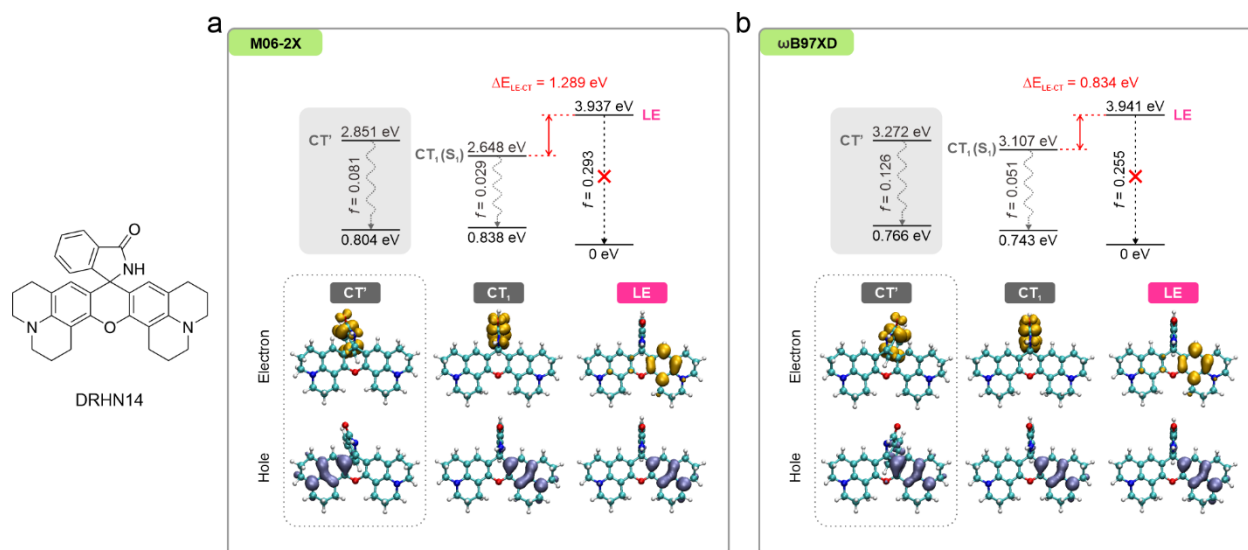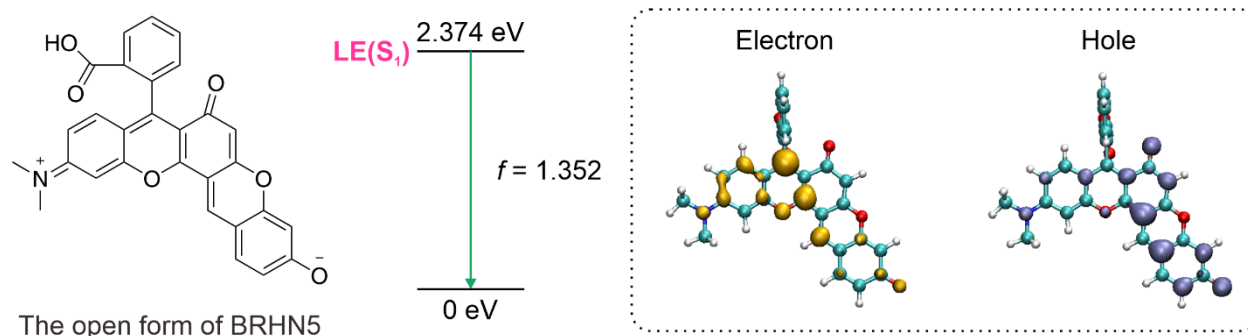

Figure S18. Molecular structure, energy levels, and the corresponding electron and hole distributions in the AES of BRHN28. The dihedral angles of 5-4-3-9, 1-2-3-6, 5-4-9-8, and 1-2-6-7 in the CT_1 state are fixed to the values in the FC state.
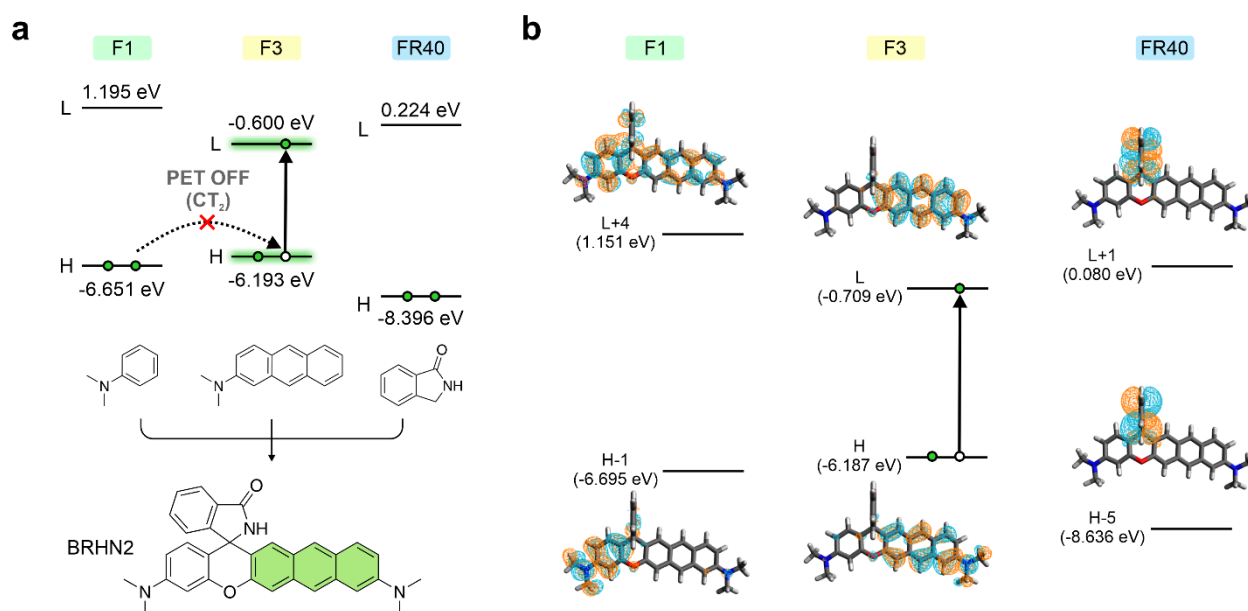
12

Figure S19. (a) Three fragments, their HOMO and LUMO energy levels in the ground state, and (b) the corresponding distributions and energy levels of the molecular orbitals in the ground state of BRHN5.
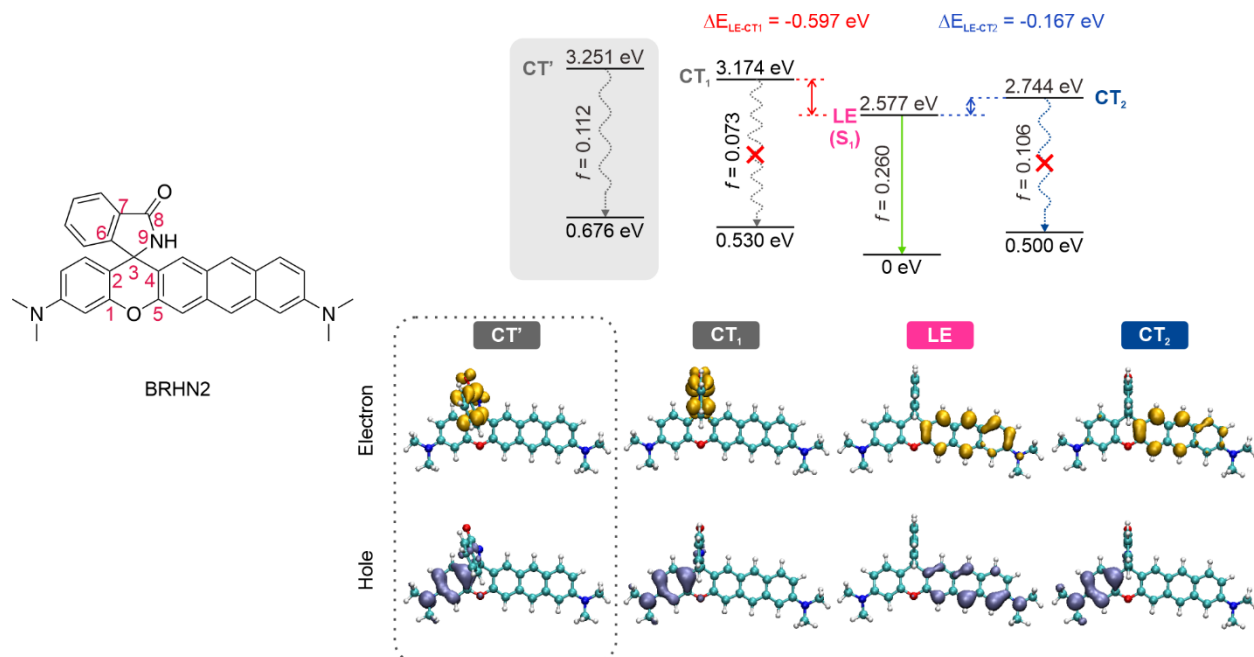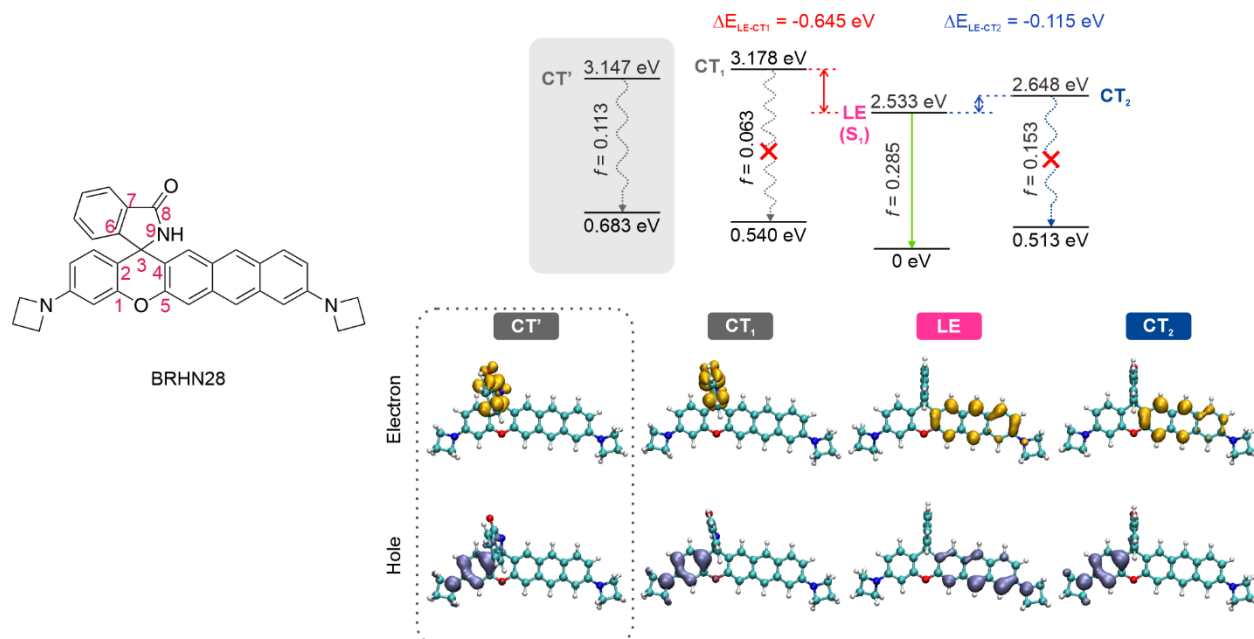

Figure S20. Molecular structure, energy levels, and the corresponding electron and hole distributions in the AES of BRHN5. The dihedral angles of 5-4-3-9, 1-2-3-6, 5-4-9-8, and 1-2-6-7 in the CT_1 state are fixed to the values in the FC state. CT_2 denoted the CT state from the F1 fragment to the F27 fragment.

Figure S21. (a) Three fragments, their HOMO and LUMO energy levels in the ground state, and (b) the corresponding distributions and energy levels of the molecular orbitals in the ground state of ProbeAC.

Figure S22. Molecular structure, energy levels, and the corresponding electron and hole distributions in the AES of ProbeAC. CT_2 denoted the CT state from the F50 fragment to the F21 fragment.
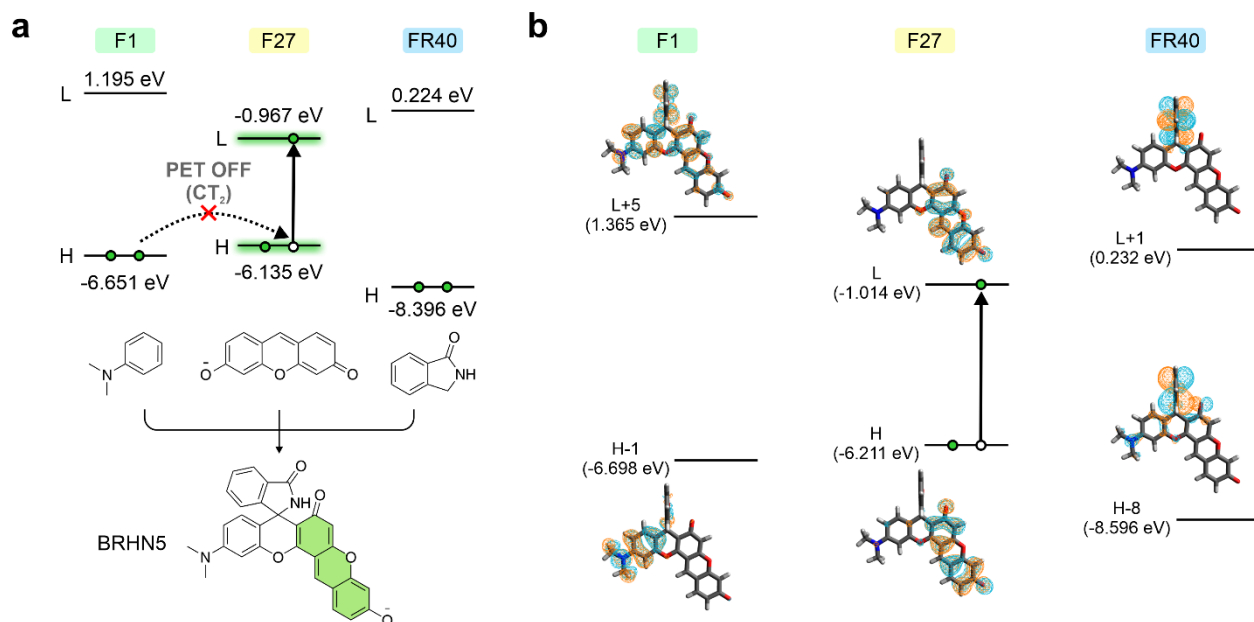
Figure S23. (a) Three fragments, their HOMO and LUMO energy levels in the ground state, and (b) the corresponding distributions and energy levels of the molecular orbitals in the ground state of RHN25_50.

Figure S24. Molecular structure, energy levels, and the corresponding electron and hole distributions in the AES of RHN25_50. CT_2 denoted the CT state from the F50 fragment to the F25 fragment.

Figure S25. (a) Three fragments, their HOMO and LUMO energy levels in the ground state, and (b) the corresponding distributions and energy levels of the molecular orbitals in the ground state of RHN21_32.
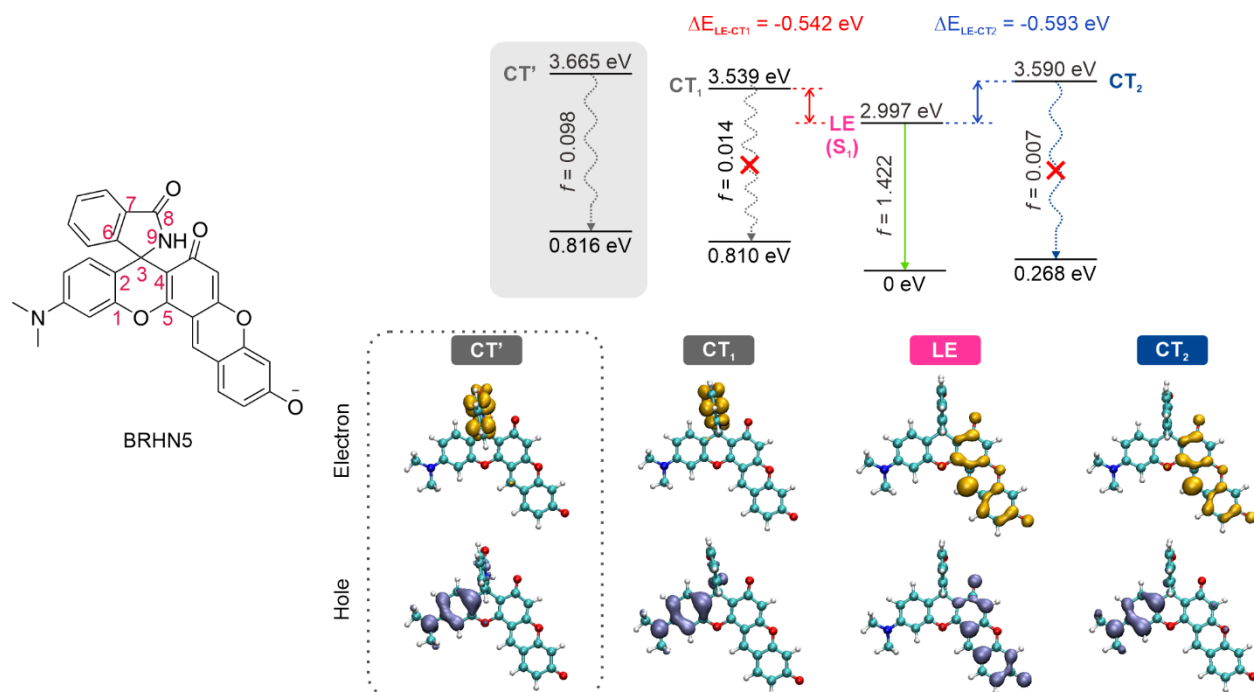

Figure S26. Molecular structure, energy levels, and the corresponding electron and hole distributions in the AES of RHN21_32. CT_2 denoted the CT state from the F21 fragment to the F32 fragment.
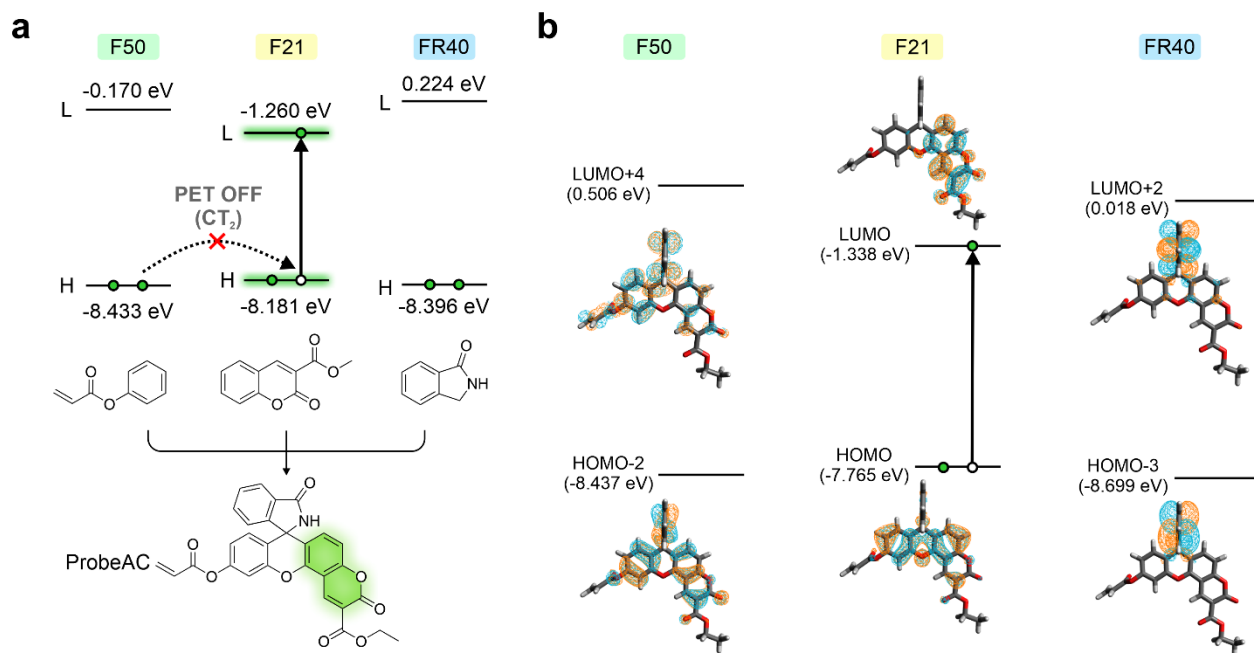
Figure S27. (a) Three fragments, their HOMO and LUMO energy levels in the ground state, and (b) the corresponding distributions and energy levels of the molecular orbitals in the ground state of BRHN1.

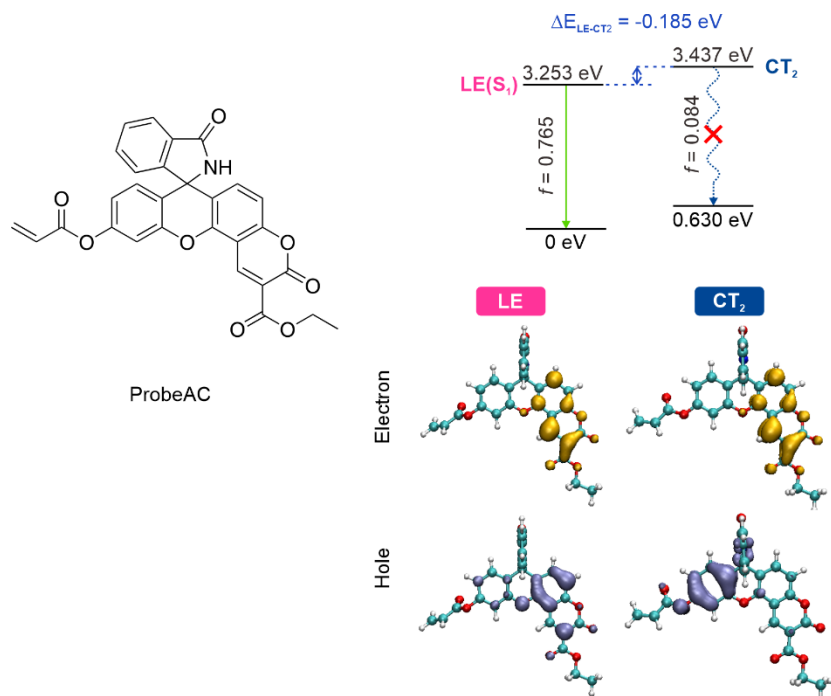

Figure S28. Molecular structure, energy levels, and the corresponding electron and hole distributions in the AES of BRHN1. The dihedral angles of 5-4-3-9, 1-2-3-6, 5-4-9-8, and 1-2-6-7 in the CT_1 state are fixed to the values in the FC state.
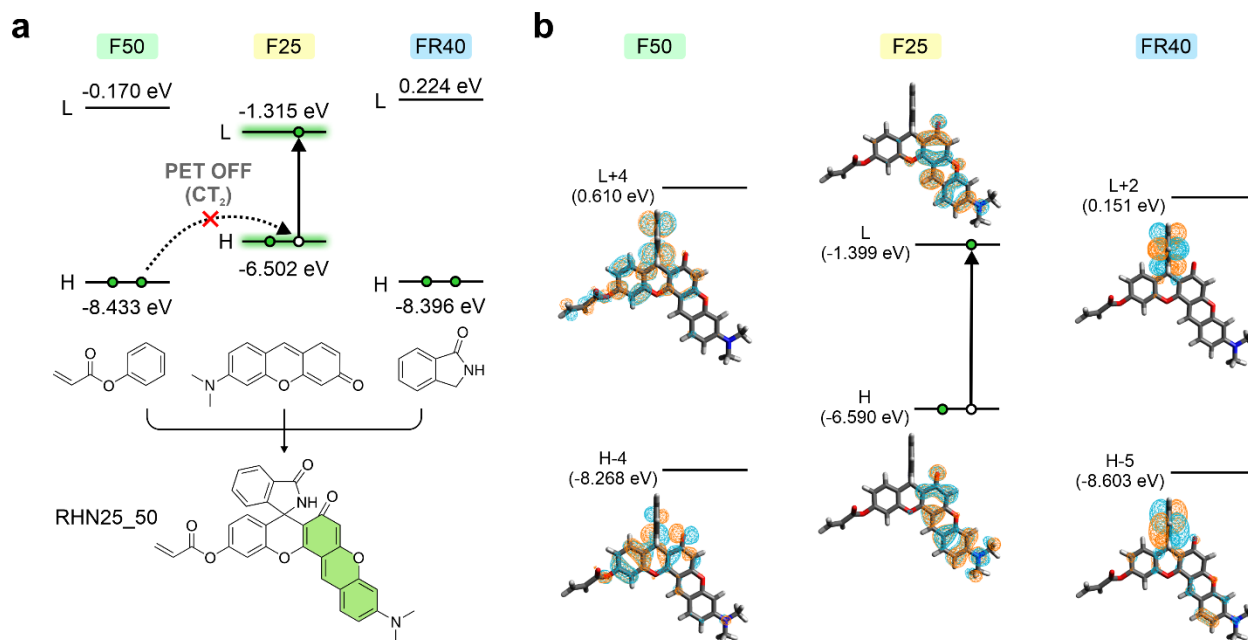
Figure S29. (a) Three fragments, their HOMO and LUMO energy levels in the ground state, and (b) the corresponding distributions and energy levels of the molecular orbitals in the ground state of BRHN3.
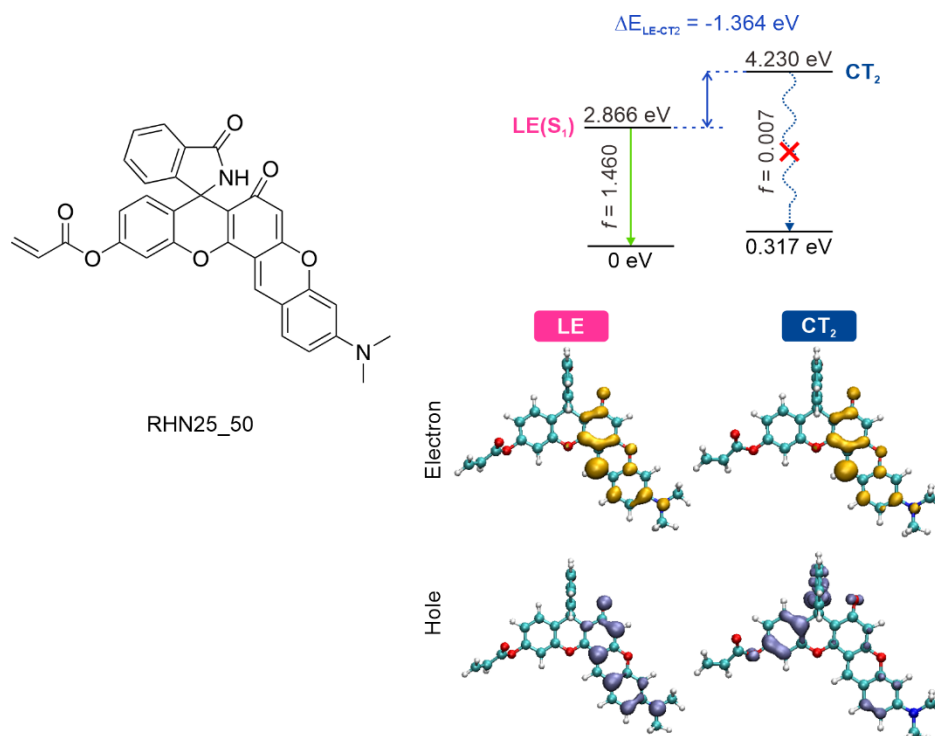

Figure S30. Molecular structure, energy levels, and the corresponding electron and hole distributions in the AES of BRHN3. The dihedral angles of 5-4-3-9, 1-2-3-6, 5-4-9-8, and 1-2-6-7 in the CT_1 state are fixed to the values in the FC state. CT_2 denoted the CT state from the F1 fragment to the F25 fragment.
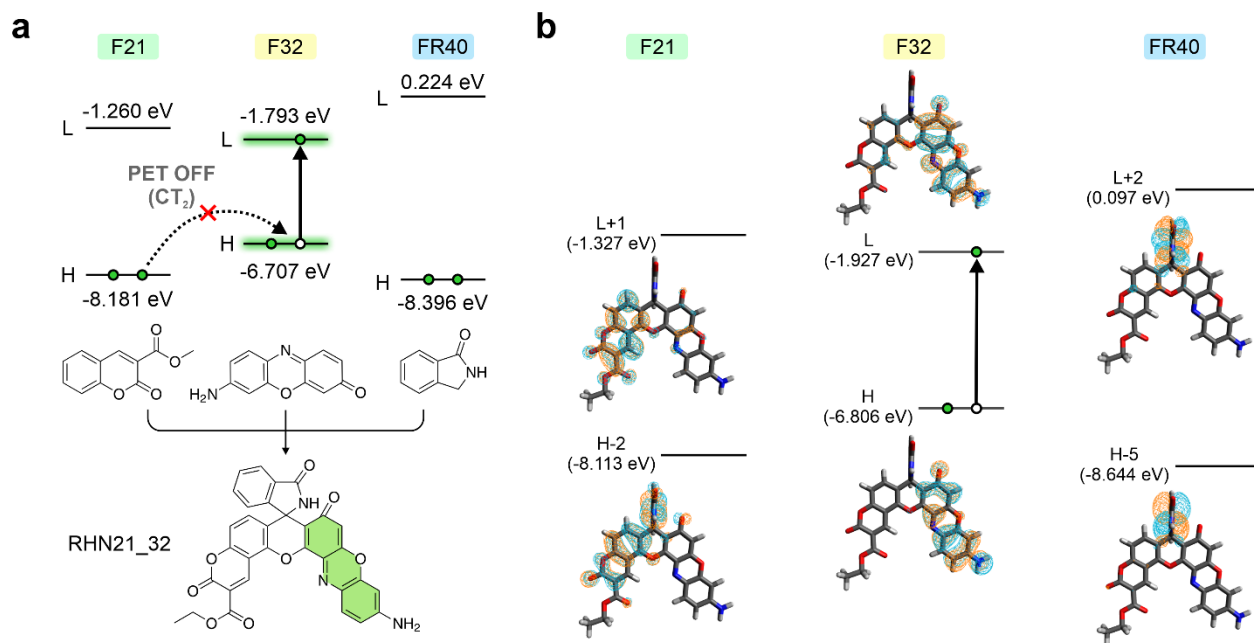
Figure S31. (a) Three fragments, their HOMO and LUMO energy levels in the ground state, and (b) the corresponding distributions and energy levels of the molecular orbitals in the ground state of BRHN4.
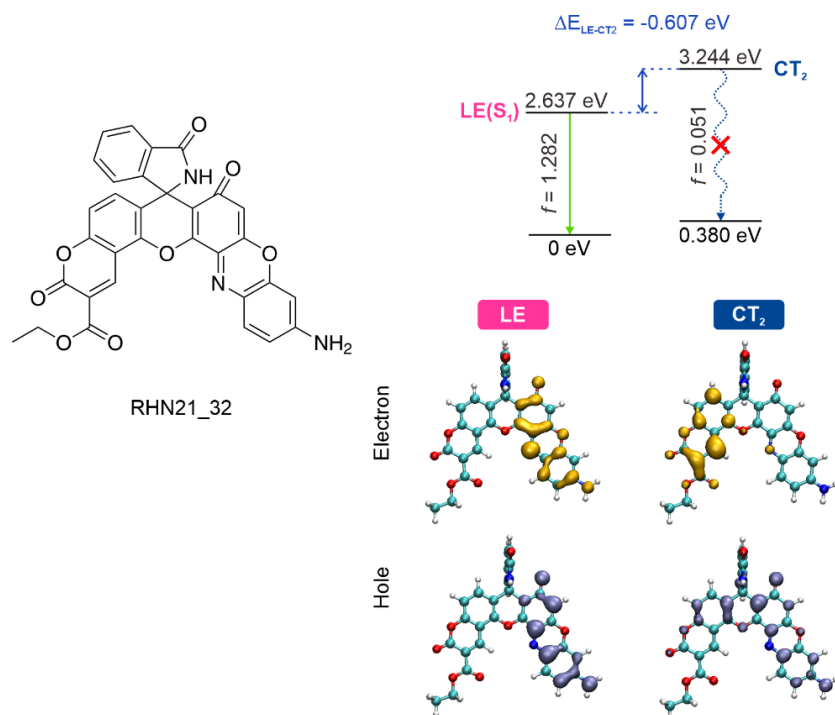

Figure S32. Molecular structure, energy levels, and the corresponding electron and hole distributions in the AES of BRHN4. The dihedral angles of 5-4-3-9, 1-2-3-6, 5-4-9-8, and 1-2-6-7 in the CT_1 are fixed to the values in the FC state. CT_2 denoted the CT state from the F1 fragment to the F26 fragment.
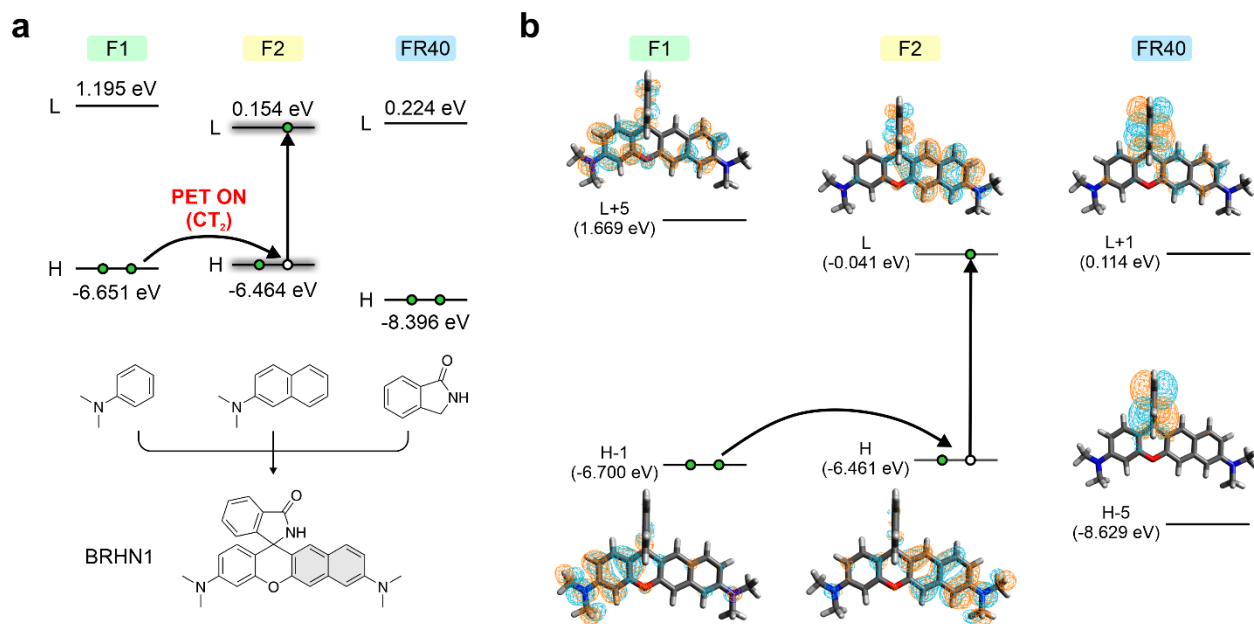
Figure S33. (a) Three fragments, their HOMO and LUMO energy levels in the ground state, and (b) the corresponding distributions and energy levels of the molecular orbitals in the ground state of BRHN6.
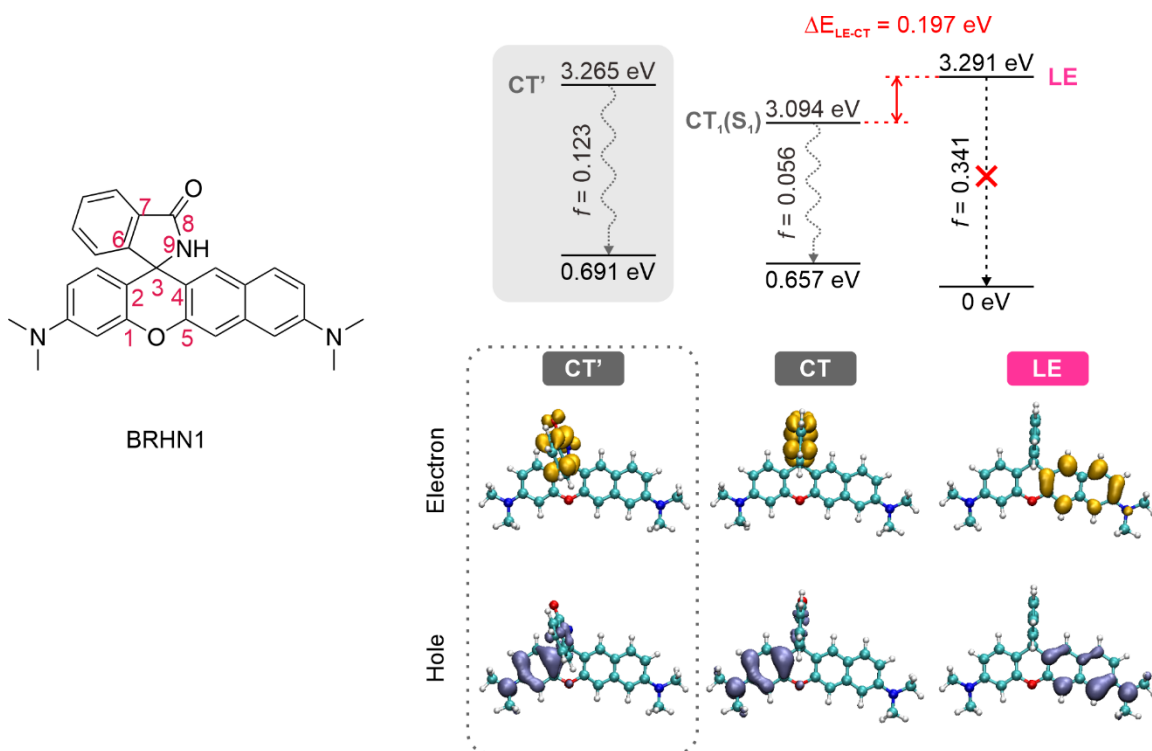

Figure S34. Molecular structure, energy levels, and the corresponding electron and hole distributions in the AES of BRHN6. The dihedral angles 5-4-3-9, 1-2-3-6, 5-4-9-8, and 1-2-6-7 in the CT$_1$ are fixed to the values in the FC state. CT$_2$ denoted the CT state from the F1 fragment to the F11 fragment.
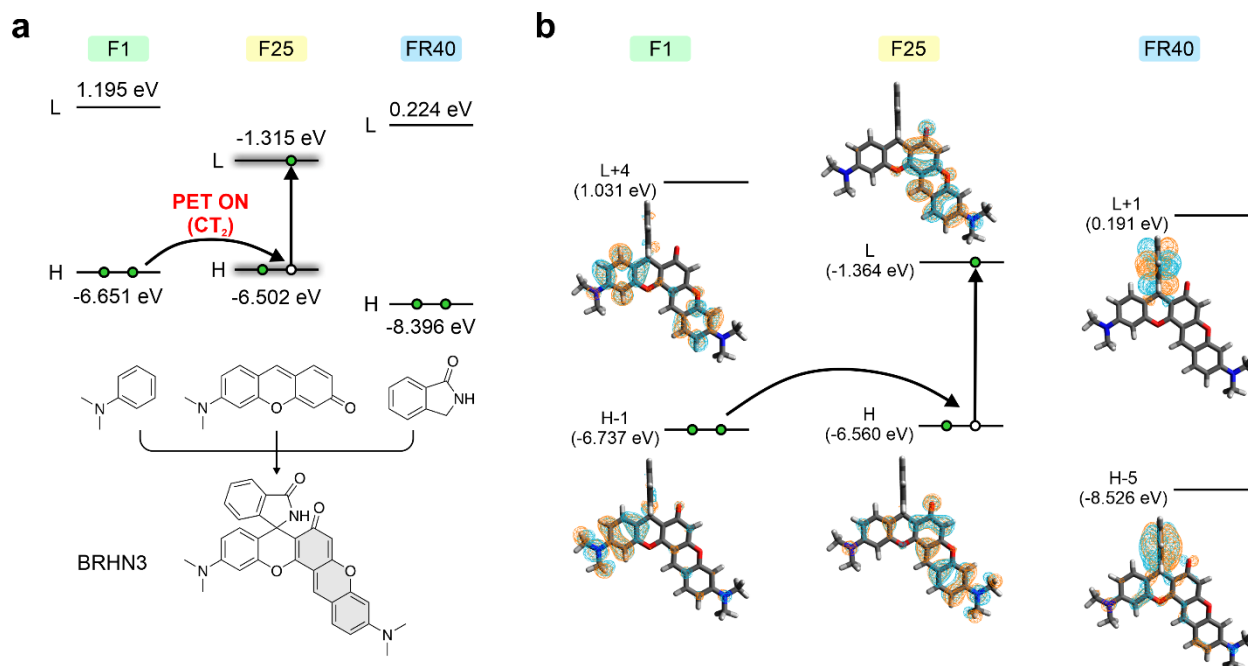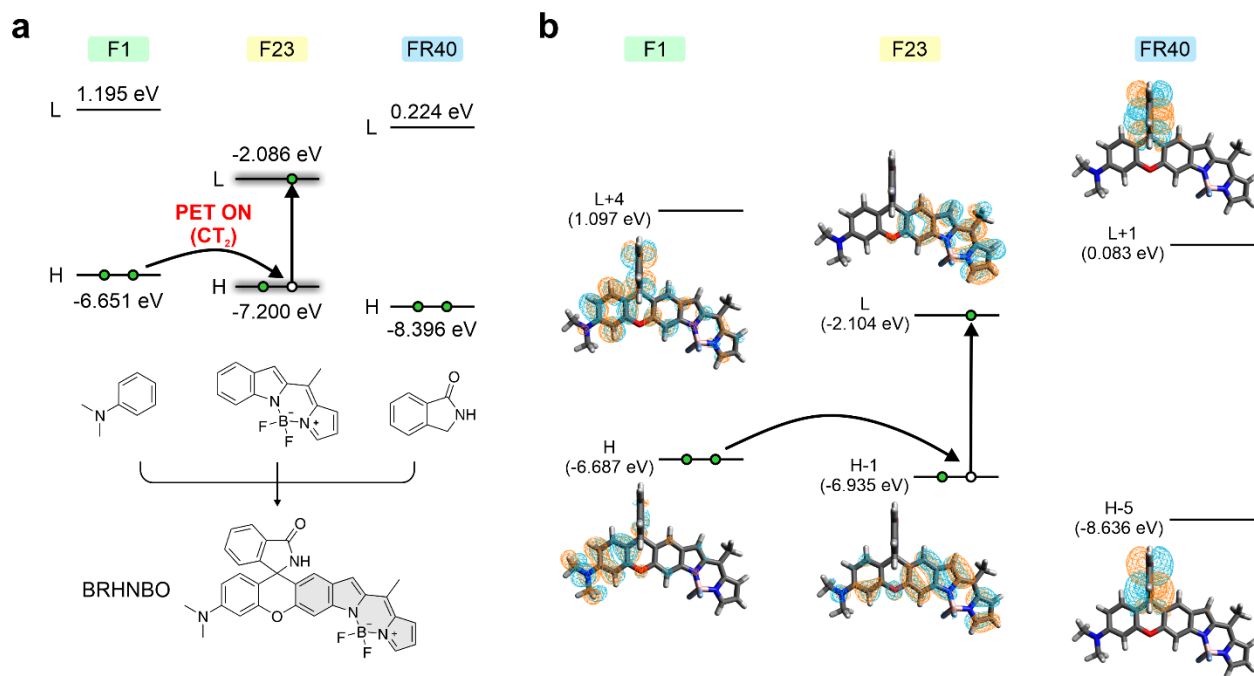
Figure S35. (a) Three fragments, their HOMO and LUMO energy levels in the ground state, and (b) the corresponding distributions and energy levels of the molecular orbitals in the ground state of BRHNBO.
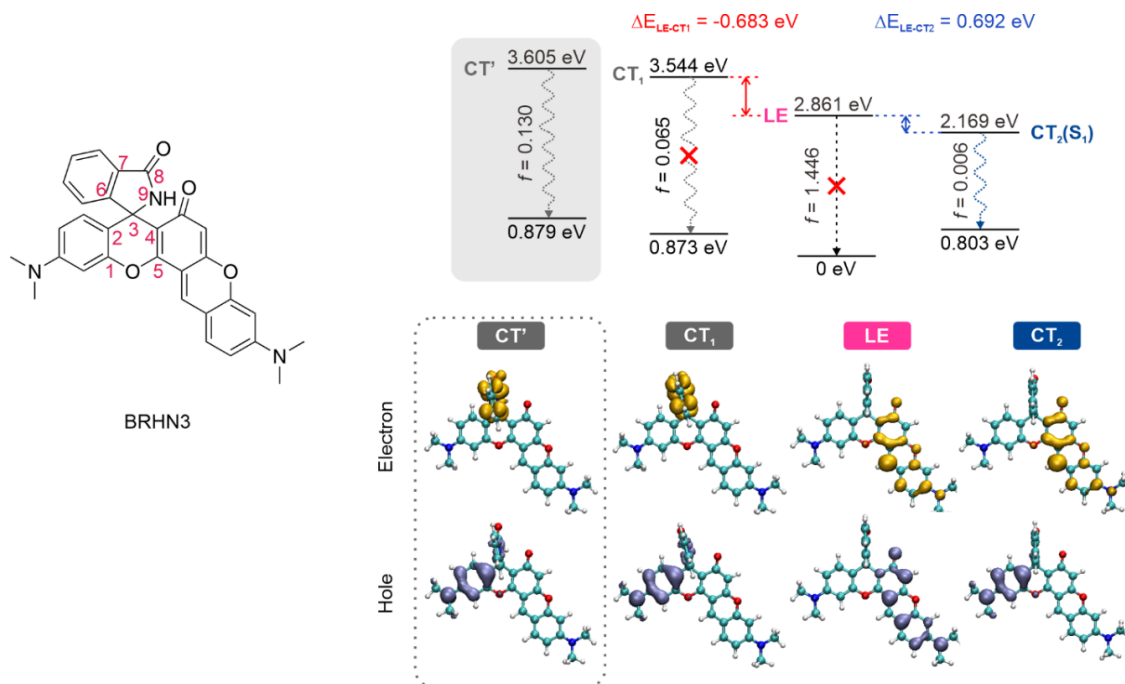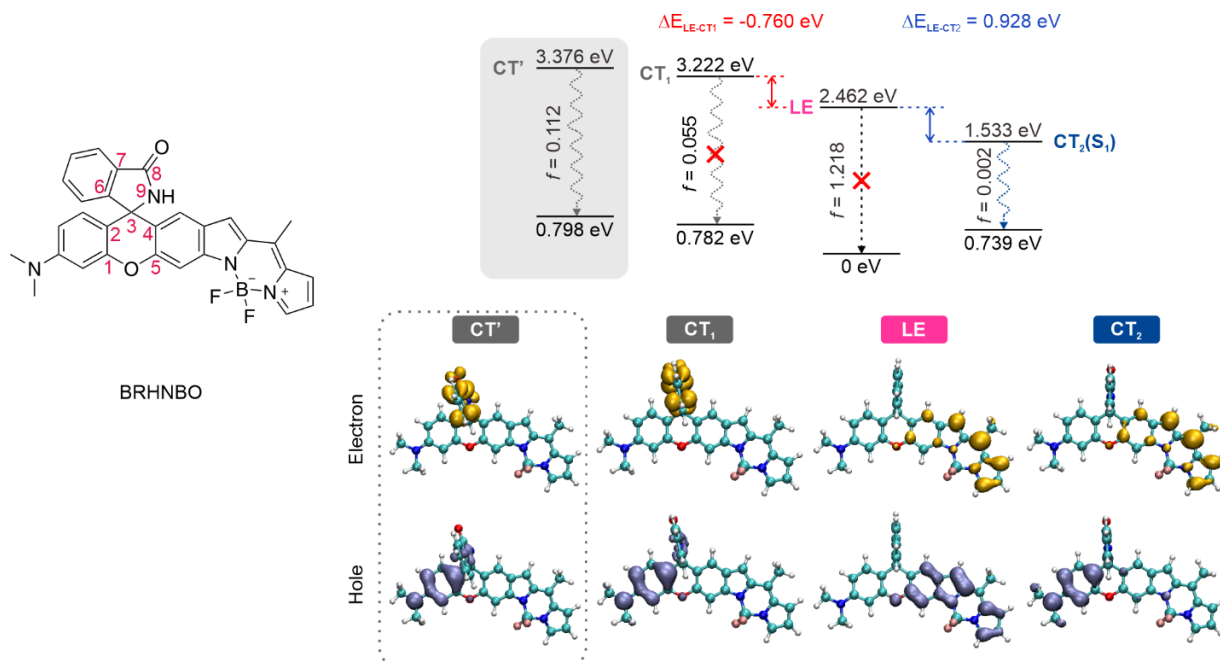

Figure S36. Molecular structure, energy levels, and the corresponding electron and hole distributions in the AES of BRHNBO. The dihedral angles of 5-4-3-9, 1-2-3-6, 5-4-3-6, and 1-2-3-9 in the CT_1 state are fixed to the values in the FC state. CT_2 denoted the CT state from the F1 fragment to the F23 fragment.
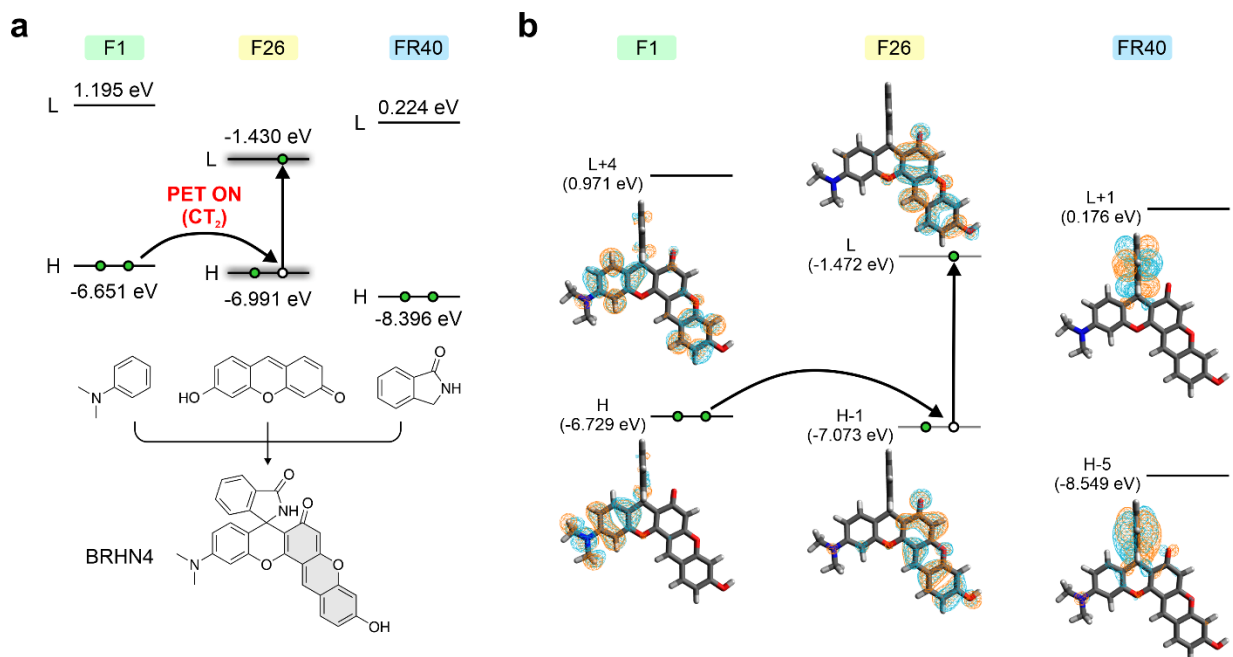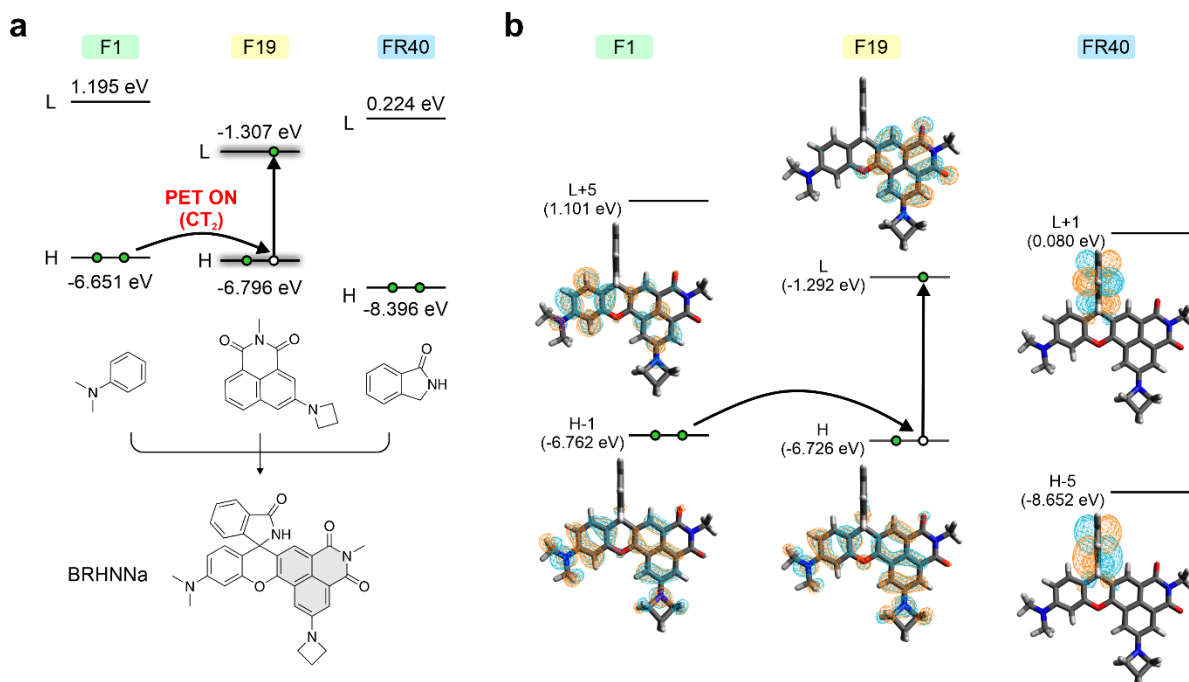
Figure S37. (a) Three fragments, their HOMO and LUMO energy levels in the ground state, and (b) the corresponding distributions and energy levels of the molecular orbitals in the ground state of BRHNNa.
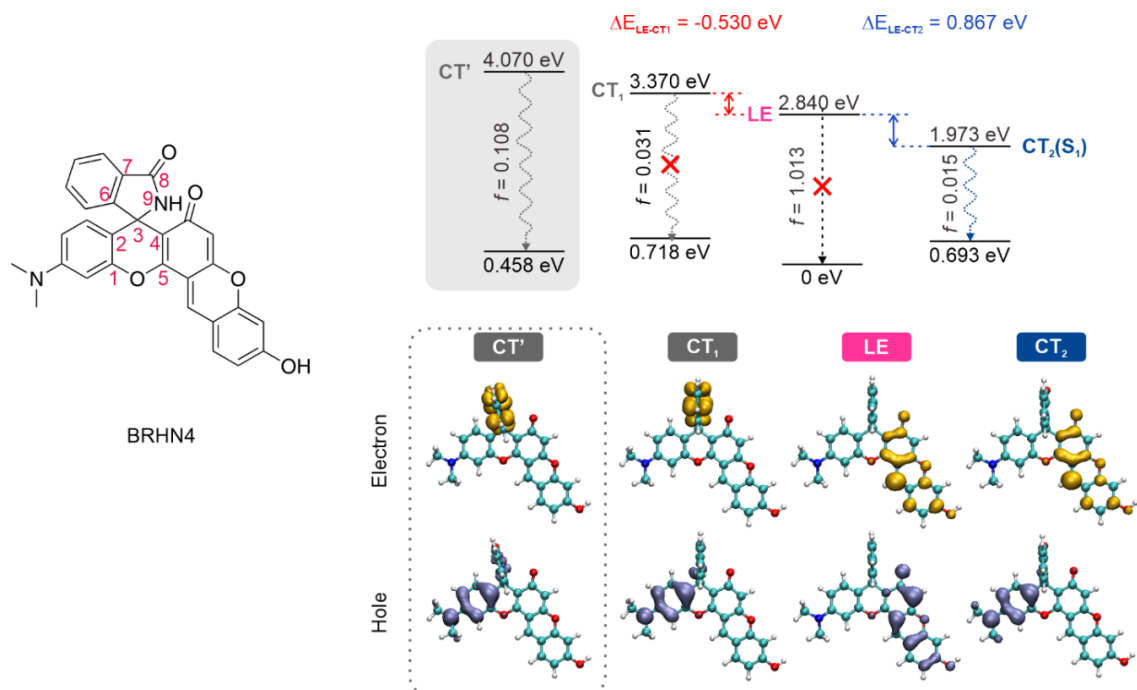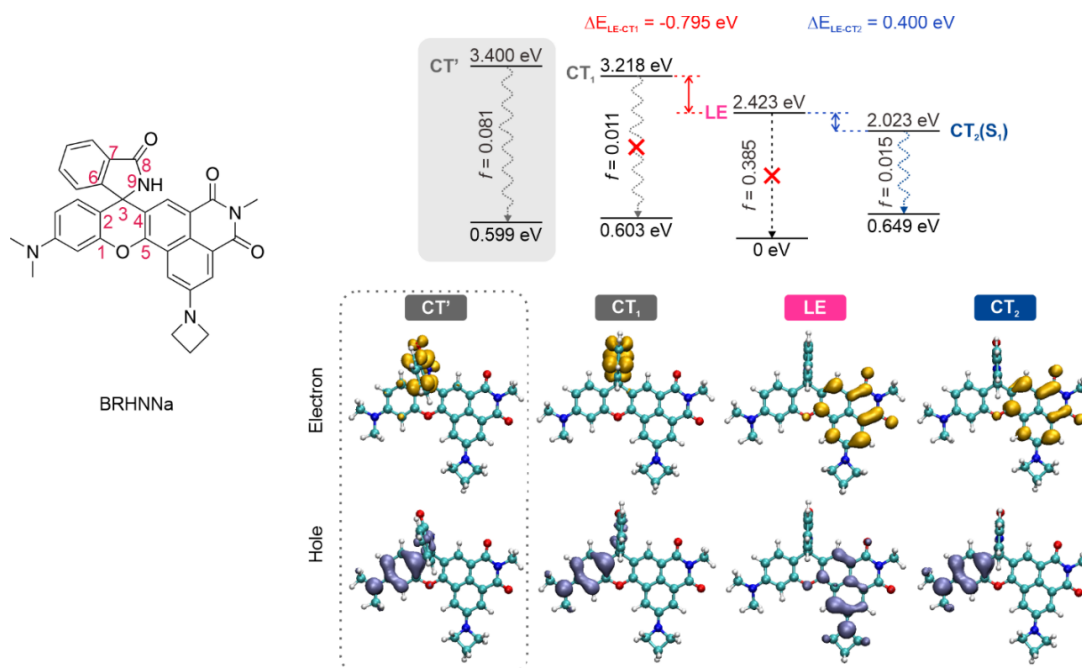

Figure S38. Molecular structure, energy levels, and the corresponding electron and hole distributions in the AES of BRHNNa. The dihedral angles of 5-4-3-9, 1-2-3-6, 5-4-9-8, and 1-2-6-7 in the CT_1 state are fixed to the values in the FC state. CT_2 denoted the CT state from the F1 fragment to the F19 fragment.
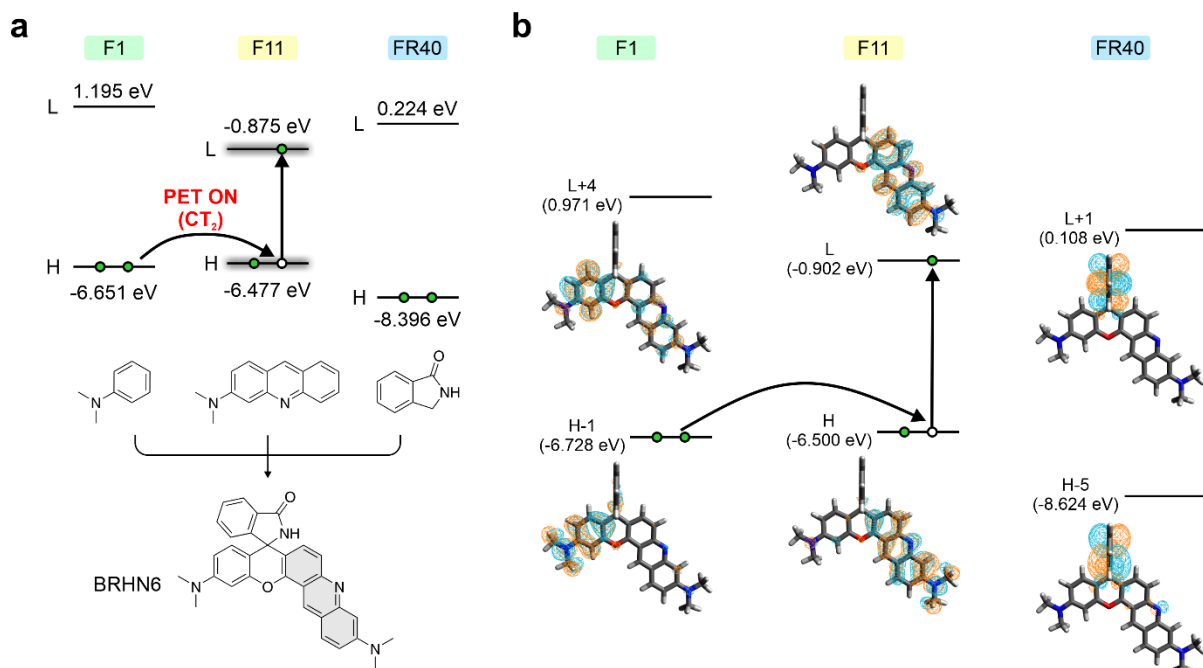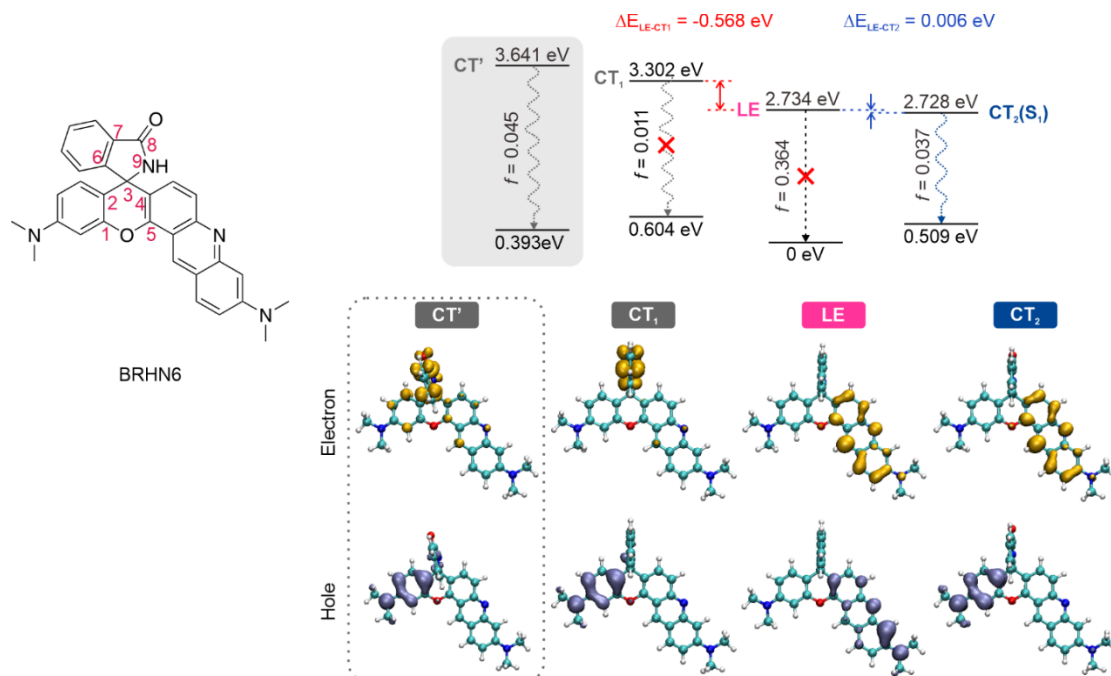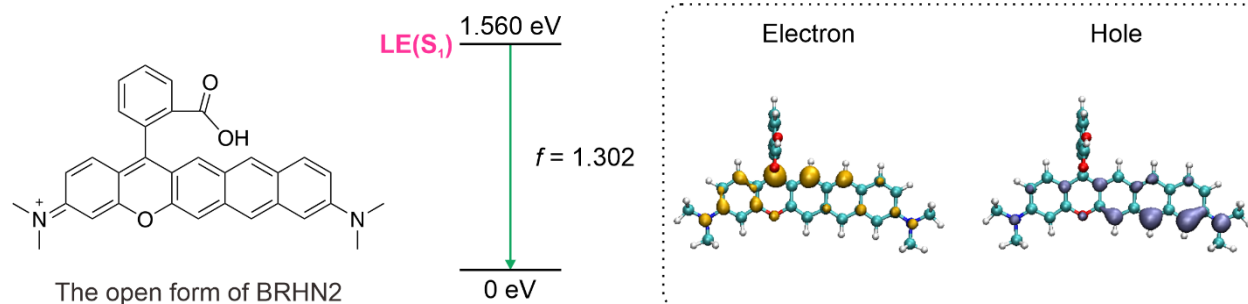
Figure S39. The molecular structure, energy level, and the corresponding electron and hole distributions of the optimized S_1 state in the open form of BRHN2 in water.
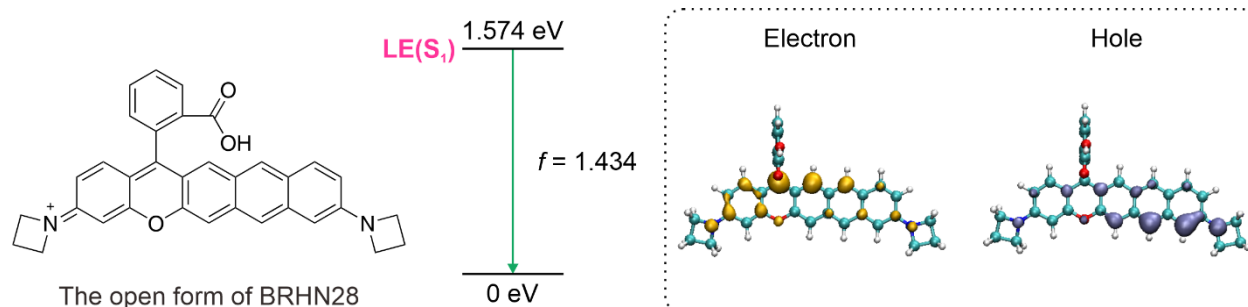
Figure S40. The molecular structure, energy level, and the corresponding electron and hole distributions of the optimized S_1 state in the open form of BRHN28 in water.
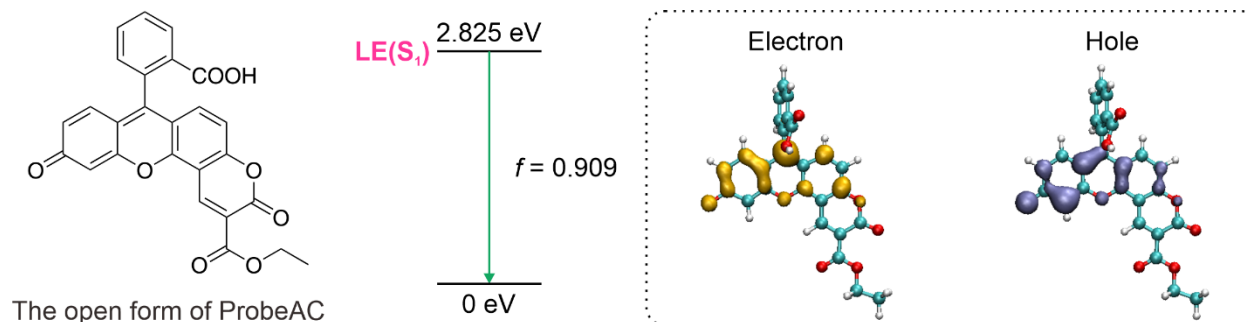
Figure S41. The molecular structure, energy level, and the corresponding electron and hole distributions of the optimized S_1 state in the open form of ProbeAC in water.
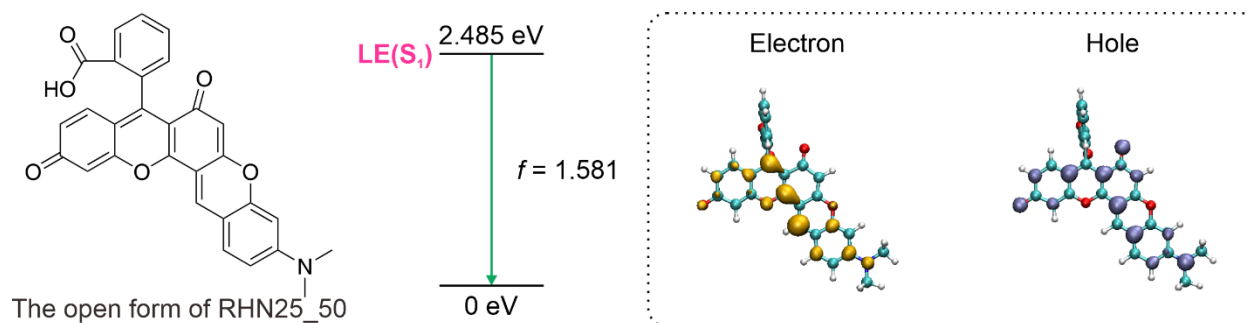
Figure S42. The molecular structure, energy level, and the corresponding electron and hole distributions of the optimized S_1 state in the open form of RHN25_50 in water.
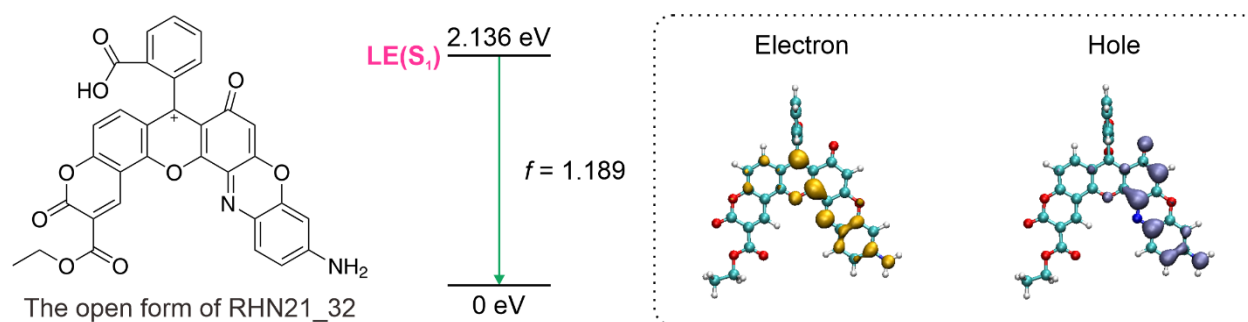
Figure S43. The molecular structure, energy level, and the corresponding electron and hole distributions of the optimized S_1 state in the open form of RHN21_32 in water.

There are two methods to define the fragment M3. One is to exclude the *meso*-carbon atom from M3 (*e.g.*, F40 in Fig. S44, Fig. S45); the other is to include the *meso*-carbon atom in M3 (*e.g.*, FR40 in Fig. S44, Fig. 4). Both methods led to similar FMOs energy levels and afforded the same conclusion on the tendency of PET. This is reasonable considering that the *meso*-carbon atom does not strongly participate in the π-conjugation of M3.
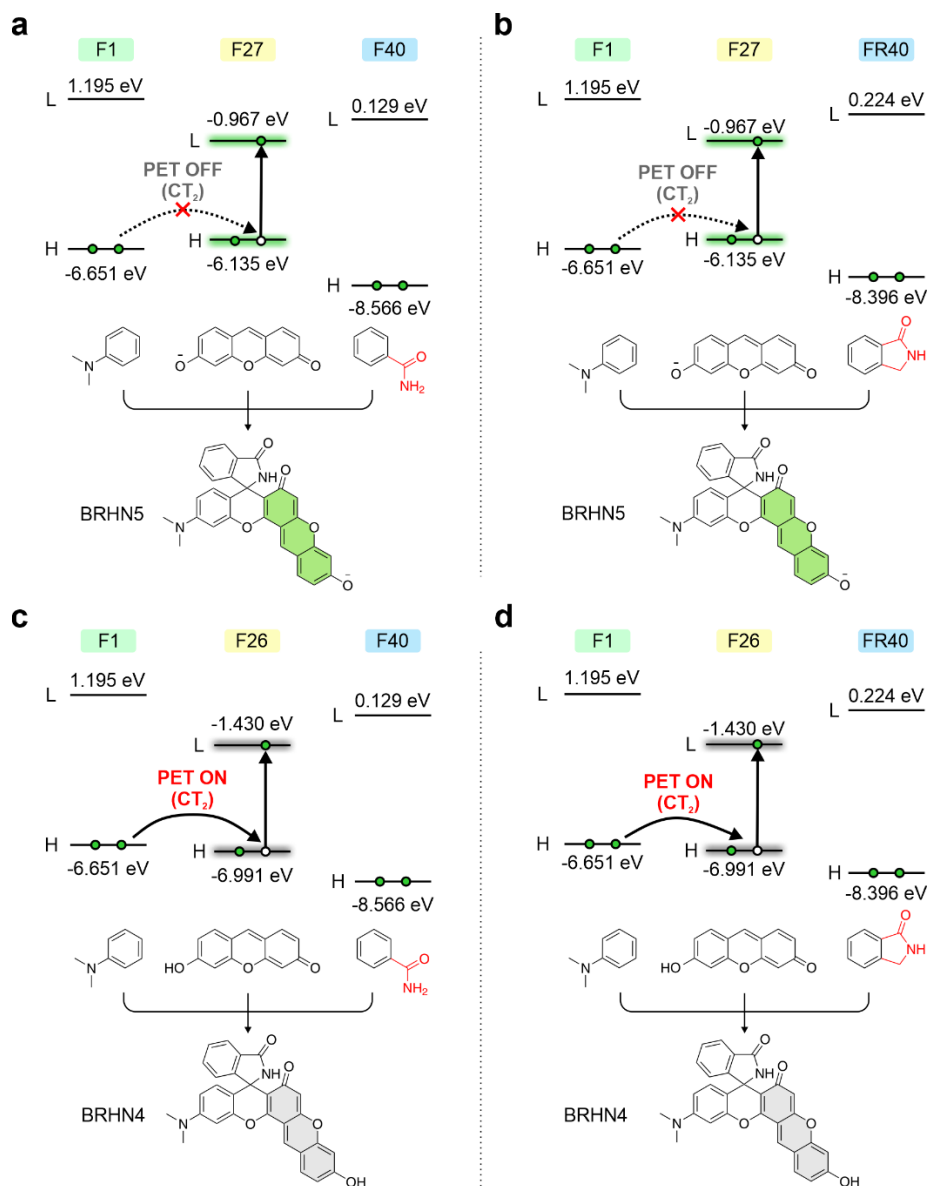
Figure S44. Three fragments (without *meso*-carbon atom from M3), their respective HOMO and LUMO energy levels in the ground state of (a) BRHN5 and (c) BRHN4. Three fragments (with *meso*-carbon atom from M3), their respective HOMO and LUMO energy levels in the ground state of (b) BRHN5 and (d) BRHN4.

Figure S45. Calculated HOMO and LUMO energy levels in the ground state of M1&M2 fragments in Fig.3a and different M3 fragments (without the meso-carbon atom) using different functionals: CAM-B3LYP (top), M06-2X (middle) and B3LYP (bottom) with the def2SVP basis set in water.

Table S1. The D_{CT} indexes of the LE and several CT states as well as the dipole moment in CT_1 of all rhodamines and analogs in this work.

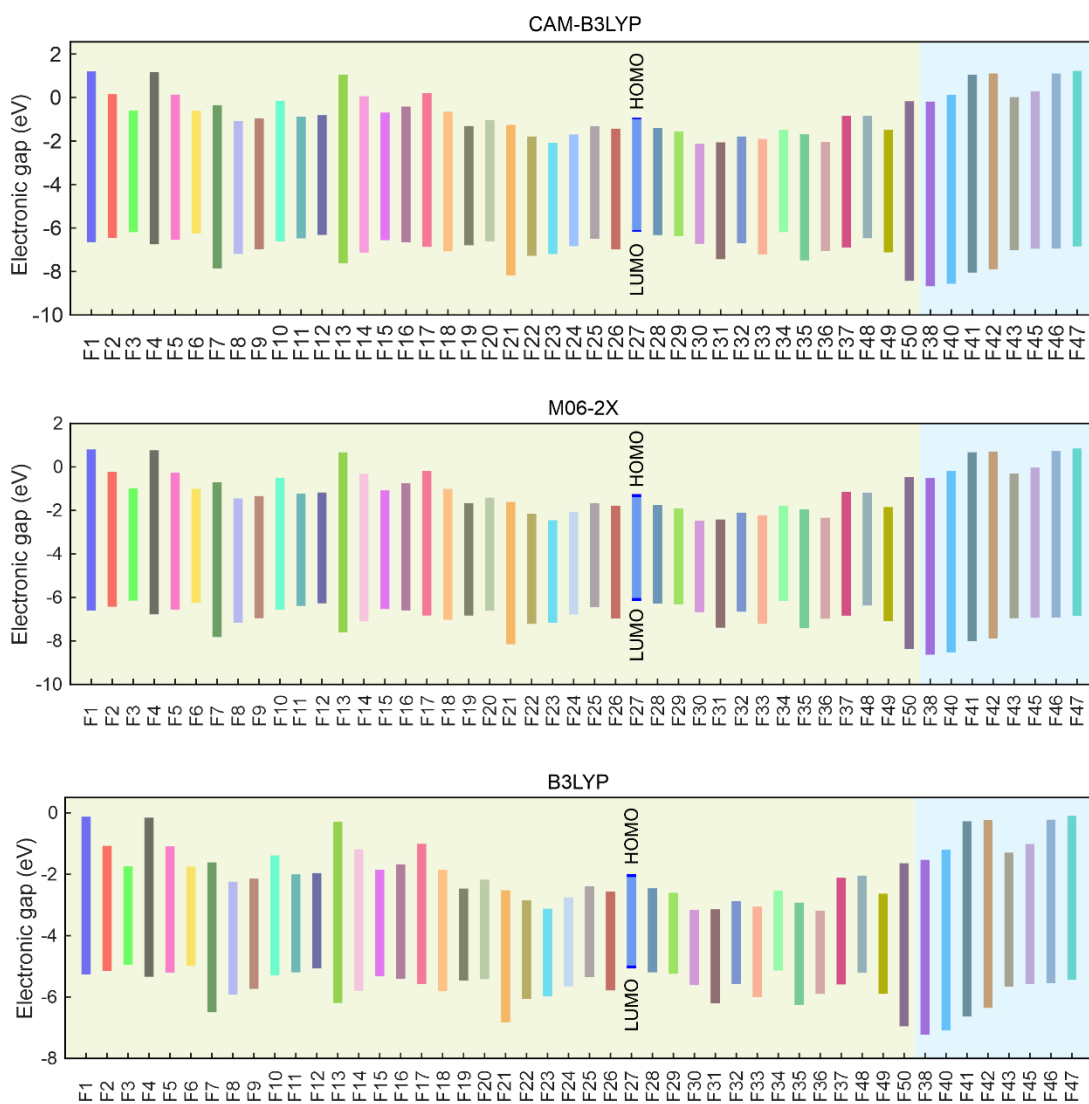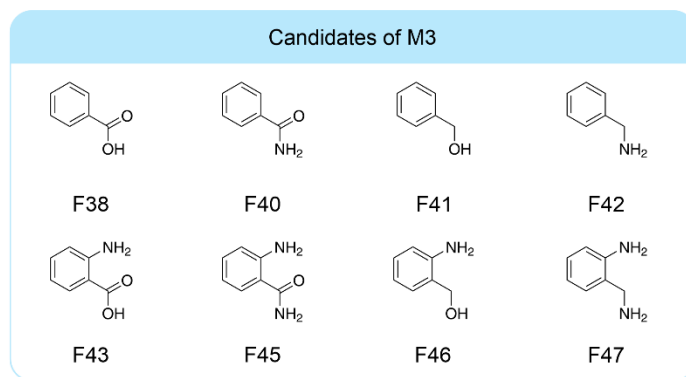|	D_{CT} indexes in CT' (Å)	D_{CT} indexes in CT_1 (Å)	D_{CT} indexes in LE (Å)	D_{CT} indexes in CT_2 (Å)	Dipole moment in CT_1(Debye)
DRHN1	3.689	4.545	1.51		24.969988
DRHN2	3.722	4.328	1.122		26.274961
DRHN3	3.493	4.413	1.281		24.122234
DRHN9	4.124	5.181	2.189		25.427926
DRHN10	3.751	4.035	1.425		19.015353
DRHN11	3.455	4.318	0.955		23.068285
DRHN12	3.73	4.74	1.511		25.244802
DRHN13	3.907	4.833	1.353		25.941538
DRHN14	3.954	5.135	1.463		26.670739
DRHN16	3.772	4.71	1.487		25.708934
DRHN17	3.022	3.743	0.904		22.151242
DRHN19	2.837	3.083	0.137		12.363563
BRHN1	3.521	4.414	1.457		23.283754
BRHN3	4.12	4.174	0.796	5.993	37.452829
BRHN4	4.137	4.418	1.164	5.922	34.136306
BRHN6	3.103	4.496	1.563	6.07	28.103371
BRHNBO	3.54	4.216	1.471	8.273	17.420493
BRHNNa	3.446	4.575	1.924	6.352	33.20138
BRHN2	3.703	4.426	1.398	6.417	22.292755
BRHN28	3.857	4.471	1.509	6.478	30.322985
BRHN5	4.124	4.297	0.606	5.917	38.569769
ProbeAC			1.447	4.912	
RHN25_50			0.838	3.561	
RHN21_32			0.697	4.015	

Table S2. The D_{CT} indexes of the LE and several CT states as well as the dipole moment in CT_1 of DRHN14 with different functionals using def2SVP in water.

Functional	D_{CT} indexes in CT' (Å)	D_{CT} indexes in CT_1 (Å)	D_{CT} indexes in LE (Å)	Dipole moment in CT_1 (Debye)
M062X	4.311	5.163	1.312	27.41854
CAM-B3LYP	3.954	5.135	1.463	26.67074
ωB97XD	3.526	5.086	1.46	25.59395

Three generations of fluorophores for single-molecule localization microscopy

Single-molecule localization (SML) can be used to achieve super-resolution imaging beyond the Abbe diffraction limit, but it requires the use of fluorophores that meet two specific criteria: sparse emission and blinking between "dark" and "bright" states.

SML fluorophores can be broadly classified into three generations. The first generation of SML fluorophores is classical fluorophores, which are mostly in "bright" states by default. These fluorophores are typically used in conventional imaging and are not specifically designed for super-resolution imaging. To meet the requirements of SML, harsh treatments such as the introduction of chemical additives and intense laser radiation are often necessary to induce sparse emissions and blinking in these fluorophores. However, these harsh treatments can compromise biocompatibility, complicate experimental preparation, photobleach dyes quickly, and cause high phototoxicity in live cells.

In the second generation of SML fluorophores, the fluorophores are mostly in the "dark" state. A small fraction of these fluorophores will turn on emissions upon photoactivation or spontaneously blinking (via thermal equilibrium between the "bright" and "dark" states). They are specifically designed for super-resolution imaging. However, photoactivable dyes may require additional hardware, such as two lasers, one for photoactivation and the other for producing fluorescence, instead of a single laser. The photoactivation laser often suffers from short wavelengths and high phototoxicity. While spontaneously blinking dyes have the potential to simplify optical setup and enable long-lasting imaging through low-power photoexcitation, significant research efforts are needed to increase the choice of emission colors, improve the blinking properties to suit heterogeneous microenvironments in live cells, and enhance the brightness during imaging. Additionally, these dyes are not suitable for conventional imaging as only a small fraction of the dyes are in the "bright" state.

We anticipate that the third generation of SML fluorophores will have dual emissions at different wavelengths, allowing for simultaneous conventional and super-resolution imaging. Conventional imaging has a fast acquisition speed but low resolution, while super-resolution imaging has a high resolution but a long acquisition time. By using conventional imaging for a general view and super-resolution imaging only in specific areas of interest, we can take advantage of both techniques. Existing rhodamines cannot perform both conventional and super-resolution imaging at the same time, but dual-emission rhodamine analogs can, by using the majority of short-wavelength emissions for conventional imaging and the minority of long-wavelength emissions for super-resolution imaging in selected regions.

The dual-emission rhodamine analogs can blink spontaneously or through controlled photoactivation using a laser that matches the UV-vis absorption peak of the closed form. These new rhodamine analogs also have an expansive π-conjugation and red-shifted UV-vis absorption in the closed form, which reduces phototoxicity in comparison to existing photoactivatable rhodamines.

In summary, the first generation of SML fluorophores is mostly "on", mainly designed for conventional imaging. The second generation of SML fluorophores is mostly "off" with sparse

and blinking emissions, specifically developed for super-resolution imaging. The third generation of SML fluorophores could switch between two distinct "on" states with different fluorescence wavelengths. By adjusting the proportion of these two states, we can achieve simultaneous conventional and super-resolution imaging, maximizing imaging efficiency.
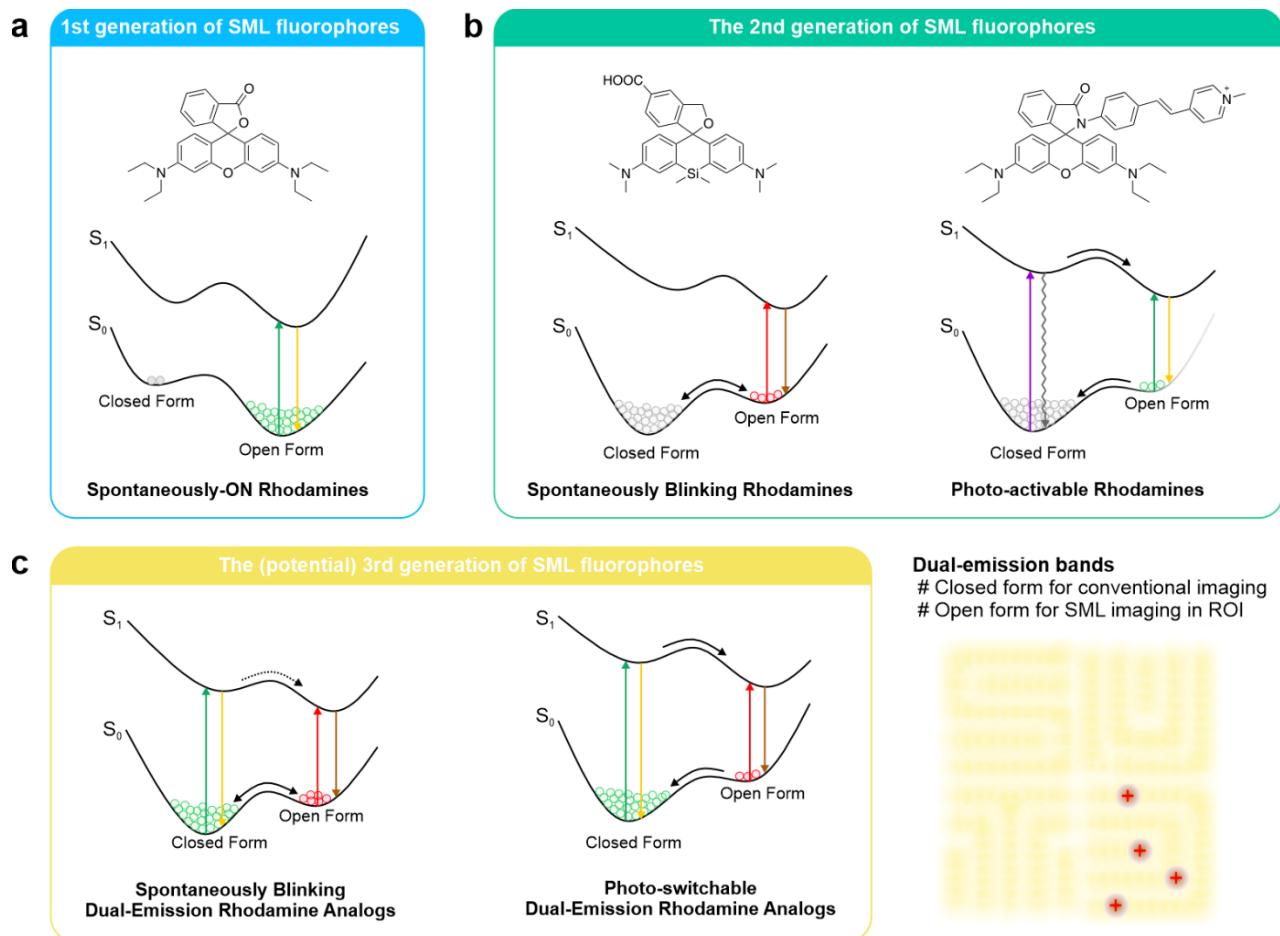

Figure S46. Schematic illustration of the potential energy surface profiles of three generations of SML fluorophores and representative compounds in the first two generations. The inset of (c) illustrates the principle of dual channel imaging: the closed form emissions enable conventional imaging, while the open form imaging allows super-resolution imaging through single-molecule localization in a region of interest (ROI).